Journal of Volcanology and Geothermal Research 421 (2022) 107418

Contents lists available at ScienceDirect

Journal of Volcanology and Geothermal Research

journal homepage: www.elsevier.com/locate/jvolgeores

The mafic Curacautín ignimbrite of Llaima volcano, Chile

Aaron A. Marshall [a,b,*], Brittany D. Brand [a], Valeria Martínez [c], Jade M. Bowers [a], Megan Walker [a], V. Dorsey Wanless [a], Benjamin J. Andrews [d], Michael Manga [e], Pedro Valdivia [a], Guido Giordano [f]

[a] Department of Geosciences, Boise State University, Boise, ID 83725, USA
[b] Department of Mineral Sciences, Smithsonian Institution, Washington, DC 20560, USA
[c] Departamento de Ciencias de la Tierra, Universidad de Concepción, Concepción, Chile
[d] Global Volcanism Program, Smithsonian Institution, Washington, DC 20560, USA
[e] Department of Earth and Planetary Science, University of California Berkeley, Berkeley 94720, CA, USA
[f] Dipartimento di Scienze della Terra, Universitá Roma Tre, Italy

ARTICLE INFO

Article history:
Received 26 May 2021
Received in revised form 18 October 2021
Accepted 20 October 2021
Available online 31 October 2021

Keywords:
Llaima
Curacautín ignimbrite
Mafic
Explosive volcanism
Microlites

ABSTRACT

Mafic volcanism accounts for 80% of magmas erupted on Earth. Although the majority of these eruptions are effusive to Strombolian and fountain-fed, large explosive mafic eruptions do occur. This work uses the deposits and pyroclast textures from the 12.6 ka Curacautín ignimbrite eruption of Llaima volcano to constrain the conditions that drove this mafic explosive eruption and extrapolate the findings to provide insights into the conditions that promote large-volume, mafic explosive volcanism elsewhere. The Curacautín ignimbrite (Ci) consists of four massive coarse ash to lapilli tuff flow units; Unit 1 is at least 30 m thick in proximal exposures, and Units 2–4 range from 1 to 4 m thick. New ^{14}C dates and field observations suggest the Ci is the result of a single eruptive episode at ~12.6 ka. A lack of fall deposits and presence of abundant clast agglutination suggests the Ci eruption was a boil over event. We estimate the proximal Ci tephra volume to be between 6 and 9 km^3 (equivalent to 3.5–4.5 km^3 DRE), which is less than previous estimates. Even with our lower estimate, the Ci is still larger than the Masaya Triple Layer, Pucón ignimbrite, Tarawera 1886, and Etna 122 BCE mafic eruptions.

Average vesicularities of pyroclasts range from 43 to 71%, and all but one exposure have vesicularities ≤56%. Average phenocryst content is ≤1–3%, but plagioclase microlite crystallinities are between 29 and 44%, with volumetric number densities between 8.21×10^6 and 1.84×10^7 mm^{-3}. Such high microlite content suggests high disequilibrium resulting from rapid magma ascent and decompression. We interpret that the combination of rapid ascent and increased magma viscosity due to the crystallization of microlites caused gases to remain coupled with the Ci magma. This, in combination with ash textures, suggests the Ci eruption explosivity was driven by brittle fragmentation. Assuming that mass eruption rates exceeded $2.0 \times 10\,8$ kg s^{-1} to produce complete column collapse, we estimate an eruption duration of ~15–17 h. This study further supports the interpretation that extensive microlite nucleation from rapid ascent can lead to large mafic explosive eruptions.

1. Introduction

Mafic volcanism constitutes more than 80% of volcanic activity on Earth (Parfitt, 2004). These eruptions are primarily effusive to mildly explosive (Strombolian) owing to low melt viscosities that facilitate efficient segregation of gas from the melt and inhibits fragmentation. However, larger-volume, explosive mafic eruptions do occur. Well-documented cases include the 122 BCE eruption of Etna volcano, Italy (Coltelli et al., 1998; Houghton et al., 2004; Sable et al., 2006), the 1707 Hoei eruption from Mt. Fuji, Japan (Miyaji et al., 2011), the 1886 eruption of Tarawera volcano, New Zealand (Houghton et al., 2004; Sable et al., 2006; Sable et al., 2009), and the Fontana lapilli basalt, San Antonio tephra, and Masaya Triple Layer eruptions of Masaya volcano, Nicaragua (Costantini et al., 2009; Costantini et al., 2010; Bamber et al., 2020; Pérez et al., 2020). The latter produced scoria fall deposits. Rarer still are ignimbrite-forming mafic eruptions such as the large-volume tephritic ignimbrites of Colli Albani volcano, Italy (Giordano et al., 2006; Freda et al., 2011; Vinkler et al., 2012), the Lican ignimbrite of Villaricca volcano, Chile (Lohmar et al., 2007), the La Garrotxa volcanic field, Spain (Martí et al., 2017), and ignimbrites from Nakadake, Aso volcano (Miyabuchi et al., 2006) and Fuji volcano, Japan (Yamamoto et al., 2005). The processes that generate these uncommon eruptions remain enigmatic because their behavior seemingly contradicts accepted volcanic conventions about the processes that lead to fragmentation

* Corresponding author at: Department of Geosciences, Boise State University, Boise, ID, 83725, USA.
E-mail address: aaronmarshall410@u.boisestate.edu (A.A. Marshall).

https://doi.org/10.1016/j.jvolgeores.2021.107418
0377-0273/

(e.g., Papale, 1999). Therefore, investigating the deposits of mafic explosive and ignimbrite-forming eruptions may help improve our understanding of the conditions that promote these rare, yet devastating, events.

Much of our understanding of explosive eruptions comes from analyses of their eruptive products (Houghton and Gonnermann, 2008). Investigations of deposit distribution and granulometry can reveal fragmentation mechanism (Heiken and Wohletz, 1985), depositional processes (Branney and Kokelaar, 2002), and environmental conditions at the time of the eruption (White and Valentine, 2016). Vesicle textural studies in 2D (Shea et al., 2010), 3D (Degruyter et al., 2010; Giachetti et al., 2011; Baker et al., 2012a; Carey et al., 2013), and 4D (Baker et al., 2012b) inform the state of magmatic volatiles prior to and during an eruption. Similar studies of microlites yield insights into magma decompression and ascent rates (Szramek et al., 2006; Szramek, 2016), undercooling and supersaturation (Hammer and Rutherford, 2002; La Spina et al., 2016; Befus and Andrews, 2018; Arzilli et al., 2019), and magma viscosity (Di Genova et al., 2020). These types of analyses are incorporated into models of volcano processes to improve our understanding of the magmatic and crustal conditions that drive explosive eruptions (Cashman and Giordano, 2014; Befus and Andrews, 2018; Moitra et al., 2018; Arzilli et al., 2019; Andrews and Befus, 2020).

The Curacautín ignimbrite (Ci) in southern Chile is a voluminous, mafic pyroclastic deposit generated by Llaima volcano in the late Pleistocene (Fig. 1, Naranjo and Moreno, 1991; Naranjo and Moreno, 2005; Lohmar, 2008). Naranjo and Moreno (1991) estimated a tephra volume of 24 km^3 (Naranjo and Moreno, 1991), making the Ci potentially one of the largest, yet least studied large-volume, mafic explosive eruptions. As such, the magmatic conditions that resulted in this explosive eruption are poorly constrained. The objectives of our study are to use the deposit distribution, stratigraphy, and ^{14}C dating to determine how many eruptive episodes are associated with the Ci, refine the volume estimate, and use pyroclast textures to investigate the conditions that drove the eruption(s). Finally, we offer a conceptual eruption model for the Ci.

1.1. Geologic background

1.1.1. Geologic setting

Llaima volcano (Fig. 2; 38°41′45 S, 71°43′54 W) is a Quaternary stratovolcano in the Southern Volcanic Zone of Chile. Llaima is positioned along the NE-SW trending Liquiñe-Ofqui fault zone (Cembrano and Lara, 2009). With a volume of ~400 km^3 and a peak elevation of 3125 m (Naranjo and Moreno, 2005), Llaima is one of the largest Andean volcanoes (Völker et al., 2011). Llaima erupts approximately every seven years and has erupted 54 times since 1640 (Dzierma and Wehrmann, 2010) making it one of the most active Andean volcanoes as well. Modeling by Dzierma and Wehrmann (2010) predicts Llaima will have another VEI ≥ 2 eruption within the next 20 years with a > 90% probability.

1.1.2. Eruptive history

Llaima volcanism began ~185 ka with an ancestral shield volcano (Naranjo and Moreno, 1991). Ancestral deposits are poorly preserved due to heavy erosion during the Llanquihue glaciation (Stern, 2004; Lohmar et al., 2006). The onset of Llaima's postglacial activity is marked by the large-volume, mafic explosive eruption(s) that produced the extensive Ci (Naranjo and Moreno, 1991; Naranjo and Moreno, 2005; Lohmar, 2008). Previous carbon dates from the Ci stratigraphy suggest two eruptions, one at ~13.2 thousand years BP and another at ~12.6 thousand years BP (Naranjo and Moreno, 1991; Lohmar, 2008).

The younger deposits overlying the Ci consist of reworked Ci material and paleosols. At 10.45 thousand years BP, Llaima produced a Plinian eruption of dacitic composition that is capped by surge deposits of the same eruption (Schindlbeck et al., 2014). The subsequent ten thousand years of deposits are composed of minor tephra falls, lava flows, and paleosols from Holocene cone building. Llaima's most recent eruption was a period of Strombolian explosions from 2008 to 2009 that generated tephra fall and minor lava flows (Ruth et al., 2016; Franco et al., 2019).

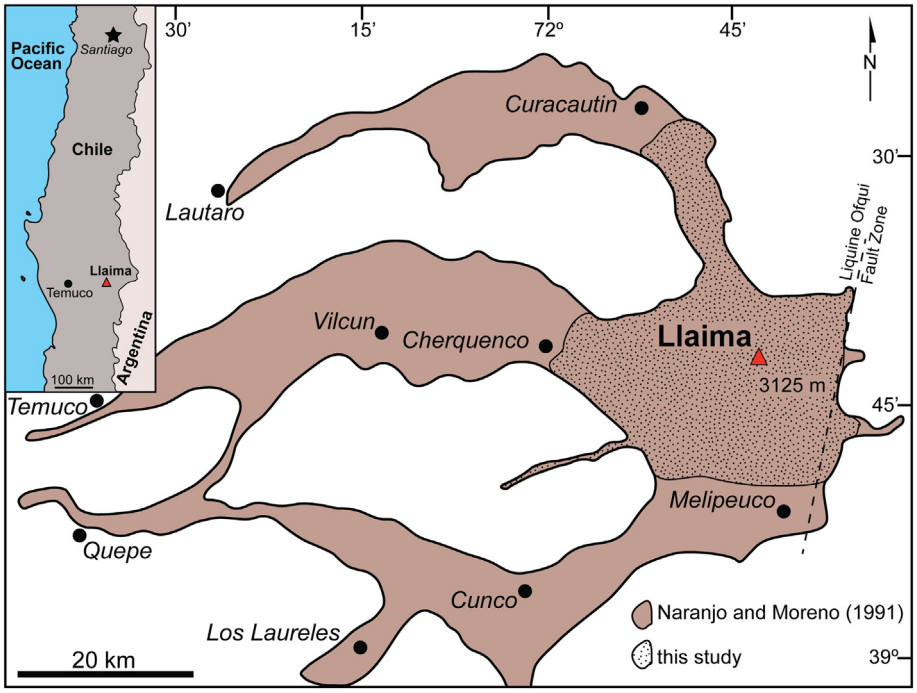

Fig. 1. Original mapped extent of the Curacautín ignimbrite by Naranjo and Moreno (1991) and the approximate extent mapped in this study (stippled pattern). Red triangle represents the location of Llaima. Temuco is ~100 km west of Llaima.

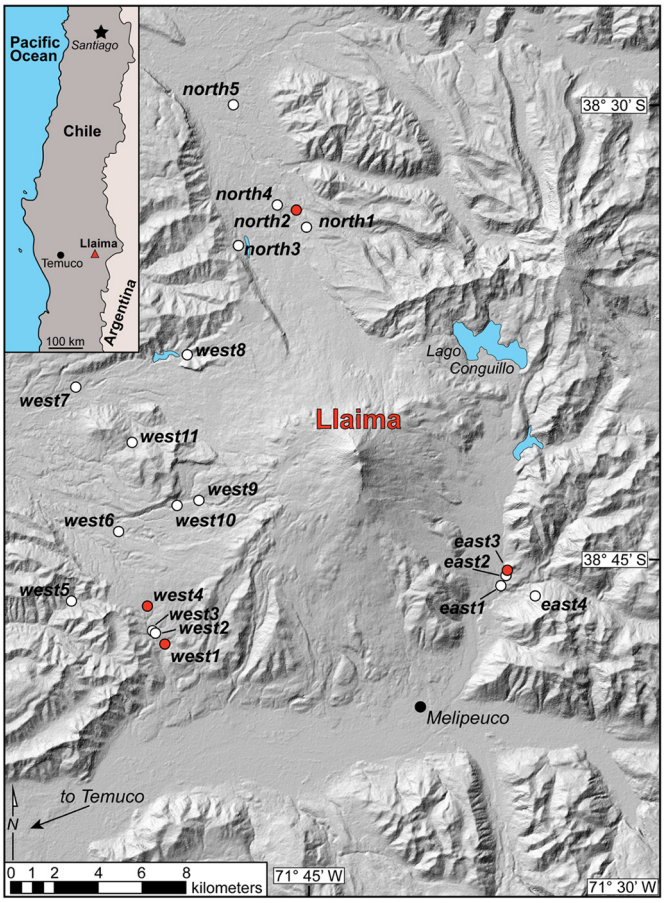

Fig. 2. Shaded relief map of Llaima volcano. Sample locations investigated in this study are plotted as white circles. Red sample points represent locations where we collected charcoal for radiocarbon dating. Digital elevation model courtesy of http://www.ide.cl/index.php/imagenes-y-mapas-base.

1.2. Why study the Curacautín ignimbrite?

The Ci is understudied despite its potential to provide insights into mafic explosive volcanism. Naranjo and Moreno (1991) hypothesize that the 13.2 thousand years BP eruption formed an 8 km wide now buried caldera, but no clear field evidence exists to support this interpretation. Their tephra volume estimate of 24 km^3 is calculated by assuming an average thickness of 10 m for 2200 km^2 of deposits (Naranjo and Moreno, 1991). This estimate is a reasonable first order approximation, but applying new methods permits a more rigorous calculation of the eruptive volume. Naranjo and Moreno (1991) and Lohmar (2008) suggest the Ci was emplaced by two distinct eruptions based on ^{14}C ages of 13.2 thousand years BP and 12.6 thousand years BP; however, field evidence to support the time interval between two eruptions requires further investigation. Finally, the magmatic conditions that caused the explosivity of the Ci eruption have yet to be fully explored.

2. Methods

2.1. Field methods

We mapped the Ci to the north, east, and west of Llaima volcano (southern deposits are not exposed, Fig. 2). We measured stratigraphic sections at each outcrop to correlate deposits from one region to another. We collected samples for granulometry, pyroclast densities, textural analysis, and compositional analyses vertically for each stratigraphic section. We closely examined stratigraphic features to identify evidence indicative of a break in deposition, such as paleosols, coignimbrite ash, truncated elutriation pipes, reworked deposits, and erosional horizons. We also collected charcoal where present for ^{14}C dating.

2.2. Granulometry and pyroclast density analysis

We collected 31 bulk samples of ignimbrite, which includes ash, pumice, and lithics. For each sample, we gathered 20–25 kg of deposit from a clean outcrop face for granulometry. Bulk samples were sieved to −3 phi ϕ (8 mm) in the field in 1ϕ intervals (ϕ scale of Wentworth, 1922). Fine fractions were brought back to the lab, dried for 24 h at 100 °C, reweighed to correct for water weight, and sieved in 1ϕ intervals using a hammer actuated automatic sieve down to 4ϕ. The <0.063 mm (>4ϕ) fraction represents the smallest bin. The size of the five largest blocks for each sample was measured in the field. Percent blocks was measured by point counting outcrop images using *ImageJ* (Schneider et al., 2012). Componentry was counted for all grains > − 3ϕ in the field; 300 grains for size fractions -2ϕ to 1ϕ were counted in the lab using a binocular microscope.

The densities of up to 100 lapilli-size pyroclasts for a subset of samples were measured following the methods of Houghton and Wilson (1991). We sprayed clasts with a waterproofing sealant that adds negligible mass to each clast. Clasts from each sample set representing the average density and one standard deviation above and below the average density were cut into thin sections for textural analysis.

Dense rock equivalent (DRE) density was measured using He-pycnometry at the University of Oregon and converted to vesicularity using

$$\varphi = 100 \cdot \frac{\rho_{DRE} - \rho_{clast}}{\rho_{DRE}}$$

where φ = vesicularity, ρ_{DRE} = DRE density, and ρ_{clast} = clast density (Houghton and Wilson, 1989).

2.3. Pyroclast textural analysis

For lapilli-size clasts, phenocryst contents of plagioclase, olivine, pyroxene, and FeTi oxides were measured by area counting thin section scans and correcting for sample vesicularity. We performed textural analysis using backscattered images in order to measure the area and number of plagioclase crystals. Backscattered images were collected on a FEI Teneo Field Emission Scanning Electron Microscope (FESEM) at the Boise State University Center for Materials Characterization using a beam current of 6.4 nA and 15 kV accelerating voltage. Plagioclase microlites were segmented as individual polygons in *ImageJ* (Schneider et al., 2012). Plagioclase area fraction (ϕ_{plag}) was calculated using

$$\phi_{plag} = \frac{A_{plag}}{A}$$

where A = the vesicle-free area and A_{plag} = the area of plagioclase (Hammer et al., 1999). Plagioclase number densities N_A were calculated by

$$N_A = \frac{n_{plag}}{A}$$

where n_{plag} = number of plagioclase crystals. The longest axis was measured in *ImageJ* and used to calculate mean crystal size S_m. The volumetric number density (N_V) was then calculated using

$$N_V = \frac{N_A}{S_m}$$

after Couch (2003). Only plagioclase microlite textures were measured because plagioclase is most sensitive to changes in pressure, temperature, and water content (Szramek et al., 2006) and, therefore, a suitable proxy for conduit processes.

2.4. Radiocarbon analyses

We collected charcoal where exposed for ^{14}C dating. Analyses were conducted at the Rafter Radiocarbon Laboratory of GNS Science, National Isotope Centre, New Zealand following standard procedures. Ages are reported in years BP. Calibration was done using SHCal13 (Hogg et al., 2013). One sample was collected in the east, three from the west, and two from the north (Fig. 2).

2.5. X-ray fluorescence analysis

We collected whole-rock major and trace element chemistry to investigate if a geochemical fingerprint exists between different Ci units vertically through the stratigraphy and geographically around the edifice. We conducted X-ray fluorescence (XRF) analyses using the ThermoARL AdvantXP+ sequential XRF spectrometer at the Washington State University Peter Hooper GeoAnalytical Laboratory. Juvenile material was chipped and hand-picked under a binocular microscope to remove xenoliths and phenocrysts. Picked material was ground to a fine powder using a tungsten carbide mill. Glass beads were created by fusing sample powder with a 10:1 mixture of lithium tetraborate and lithium metaborate flux. See Johnson et al. (1999) for complete methods.

2.6. Volume estimate

To revise the volume estimate of Naranjo and Moreno (1991), we used a modified version of the methods of Silleni et al. (2020). We first delineated a 0-m isopach that represents an approximation of the maximum depositional extent of the Ci. To do this, we created a 10-m evenly spaced point grid encompassing 176 km^2 of mapped Ci deposits from the Naranjo and Moreno (2005) geologic map using ESRI's ArcMap software. We did not use the ~2200 km^2 of deposits originally mapped in Naranjo and Moreno (1991) because we were unable to corroborate this area of deposition with our mapping. The farthest distance we mapped the Ci in this study is ~25 km to the north. The hillslope angle where the Ci is deposited was calculated at each point within the fishnet (17,615 total points). Three hillslopes, 9°, 13.5°, and 17.5° degrees were chosen to represent the maximum Ci extent whereby we trace a 0-m isopach. We approximate deposit thinning by measuring the change in deposit thickness between outcrops to estimate the lateral extent of Ci deposition in valleys and drainages using measured stratigraphic sections of this study and those of Lohmar (2008). We note that we only have one outcrop where the base is exposed, and this thinning is therefore assumed to be a minimum estimate. Simplified 5-m isopachs up to a maximum thickness of 35 m were manually traced based on measured sections and field observations.

3. The Curacautín ignimbrite

The Ci is exposed proximally (within ~30 km) to the north, east, and west of Llaima volcano. Naranjo and Moreno (1991) map the Ci throughout drainages to the S and SW of Llaima and as far west as the city of Temuco (Fig. 1); however, our field mapping did not locate any Ci exposures beyond those shown in Fig. 2. Therefore, we base our volume estimates on the known exposures mapped in our study and those of Naranjo and Moreno (2005).

The most complete section of the Ci is found on the east side of the modern-day edifice and contains four discernable units (outcrops east1, 2, and 3; Fig. 2). Exposures to the north and west share similar deposit characteristics to the flow units observed in the east. However, we do not find multiple flow units in these other exposures, which could be due to the lack of deposition of multiple flow units in other locations, amalgamation of flow unit contacts, or loss of data due to the incomplete and heavily eroded nature of those outcrops. As such, we use depositional characteristics, granulometry, pyroclast density, and pyroclast chemistry to try to correlate outcrops around the volcano. Sample locations and granulometric data are presented in Table 1.

3.1. Eastern stratigraphy

The most complete eruptive sequence is exposed in the eastern exposures (Fig. 3). Here, the Ci consists of four flow units of variable thicknesses. The lowest and thickest unit is Unit 1. This unit is exposed and accessible at exposures east1, east2, and east3 (Fig. 2). Units 2, 3, and 4 are considerably thinner, and only accessible at exposure east3.

3.1.1. Unit 1

Unit 1 is at least 30 m thick (base not exposed). It consists of a massive, very poorly sorted, and matrix-supported lapilli tuff with no distinct grading patterns. Faint diffuse stratification is evident throughout (Fig. 3). The exposure on average contains 1% blocks of juvenile magma (scoria) and lithics, but some localized block concentrations can be up to 3%. Lapilli and ash sized grains at the base of east1 (Fig. 2) are composed of 78% scoria and 22% lithics; lithics include mafic lavas and lesser amounts of granite and crystals. Scoria concentrations are variable upsection between 74% and 77% and decrease to 71% near the top. Granitic lithic clasts (lapilli to fine blocks in size) within the ashy matrix are platey and subangular to angular. Mdϕ for bulk samples (pyroclasts + lithics) are variable between 0.0 and 1.1 with a sorting (σ) from 2.76 to 3.01 (Table 1; Figs. 4, 5). Unit 1 slightly fines upsection (Fig. 4). There are 0.5–1 cm diameter degassing pipes in the upper 0.5 m that abruptly truncate at the contact with overlying Unit 2. The uppermost 3–6 cm contains a fine-grained ash with small spherical to ellipsoidal voids. The ash is capped with a thin (cm-thick) layer of spherical ash pellets typically 1–3 mm in diameter (Fig. 6).

Pyroclasts are subrounded, microvesicular, and often contain 1–5% of 1–5 mm diameter granitic and intermediate to mafic lithic inclusions, ≤2% phenocrysts of primarily plagioclase with lesser amounts of olivine, pyroxene, and Fe–Ti oxides, and 2–3 mm diameter crystal clots. Pyroclasts often exhibit agglomerate textures both in hand sample and in thin section (Fig. 7). Here, we use the term agglomerate to describe clasts comprising multiple pyroclasts fused together. Pyroclast groundmass is highly crystalline and microlite-rich with little to no glass (Fig. 8A). Unit 1 has ϕ_{plag} between 0.36 and 0.44, N_A between 4.99×10^4 and 6.72×10^4 mm^{-2}, and N_V between 8.21×10^6 and 1.33×10^7 mm^{-3} (Table 2). The average plagioclase microlite length is 5–6 μm. There is no systematic trend in microlite volumetric number densities with stratigraphic level. Unit 1 pyroclast densities range from 0.63 and 2.62 g cm^{-3}; average pyroclast densities are between 1.21 ± 0.23 g cm^{-3} and 1.39 ± 0.30 g cm^{-3}; there is no systematic stratigraphic trend (Fig. 4). The DRE density is 2.76 g cm^{-3}. Vesicularity varies between 50 ± 11% and 56 ± 8% with an average of 52% (Table 1).

Major and trace element chemistry are provided in Table 3. There are no systematic trends in Unit 1 major element contents stratigraphically or spatially. Unit 1 SiO_2-content ranges from 53.09–53.50 wt% (Fig. 4) and MgO-content ranges from 4.11 to 4.30 wt% (Fig. 9). Similarly, FeO-content is between 11.15 and 11.46 wt%. Total alkalis ($Na_2O + K_2O$) range from 4.05 to 4.34 wt%. CaO/Al_2O_3 ratios for Unit 1 range from 0.52 to 0.53. Unit 1 has an average Ba concentration of 198 ppm and La concentrations between 3.27 and 9.21 ppm (Fig. 10). Ce concentrations range from 14.85 to 21.57 ppm. Sr increases upsection throughout east1, east2, and east3 from 415 to 420 ppm before decreasing back to 414 ppm. Ni and Cr concentrations exhibit little variability from 10.39–13.96 ppm and 8.32–10.99 ppm, respectively. Additional trace element data is listed in Table 3.

Table 1
Curacautín granulometry and density data.

Sample	Northing	Easting	Outcrop	Unit	Elevation* (m)	Mdϕ	Sorting (σ)	F2+	F1&	Average clast density (g cm^{-3})	Average vesicularity (%)
L1	5705312	0271726	east1	Unit 1	1	0.00	3.00	16.59	56.19	1.32 ± 0.28	52 ± 10
L2	5705312	0271726	east1		3	0.00	2.99	16.84	56.82	1.35 ± 0.30	51 ± 11
L3	5705312	0271726	east1		7	1.10	3.01	21.60	63.02	1.21 ± 0.23	56 ± 8
L4	5705357	0271750	east1		14	0.75	2.75	23.12	72.49	1.31 ± 0.28	53 ± 10
L13s	5705515	0271804	east2		24.5	0.70	2.71	23.83	72.59	1.26 ± 0.25	54 ± 9
L14s	5705515	0271804	east2		25.5	0.25	2.76	18.98	68.12	1.39 ± 0.30	50 ± 11
L12	5705515	0271804	east2		28	0.50	2.59	18.58	67.71		
L6	5705558	0271863	east3		32	0.25	2.93	19.10	65.62	1.26 ± 0.27	54 ± 10
L7	5705558	0271863	east3	Unit 2	32	0.25	1.78	6.94	70.52		
L8	5705558	0271863	east3		33	0.25	2.63	19.32	69.35	1.32 ± 0.32	52 ± 12
L10	5705558	0271863	east3	Unit 3	35	0.25	2.71	13.23	64.13	1.39 ± 0.37	50 ± 13
L18	5705558	0271863	east3	Unit 4	~39	0.25	2.25	13.24	70.66	1.41 ± 0.31	49 ± 11
L16	5711555	0256269	west11	unknown	1	−1.00	2.20	4.50	50.72	1.58 ± 0.26	43 ± 10
L21	5705086	0272892	east4		1	−1.75	2.02	2.20	36.14	1.35 ± 0.32	53 ± 13
L23	5709606	0253180	west9		1	−1.75	2.30	4.24	37.87		
L24	5709266	0251805	west10		1	−2.25	2.29	3.30	28.63	1.45 ± 0.40	50 ± 18
L25	5702880	0249719	west4		1	−1.00	2.56	9.81	48.10	0.83 ± 0.25	71 ± 10
L30	5701665	0250840	west2		0.5	−0.50	2.72	12.80	57.30		
L31	5703025	0246533	west5		0.5	0.40	2.28	15.12	73.73		
L34	5727122	0257641	north2		0.5	−1.25	3.00	9.10	46.53	1.34 ± 0.24	52 ± 9
L35	5726337	0257848	north1		1	−0.60	2.50	10.00	56.21	1.43 ± 0.25	49 ± 9
L36	5726337	0257848	north1		5	−0.25	2.53	12.83	62.48	1.38 ± 0.25	50 ± 9
L37	5726337	0257848	north1		~8	−0.50	2.42	10.39	61.14	1.34 ± 0.22	52 ± 8
L38	5726093	0254449	north3		1	−0.50	2.21	7.23	59.74		
L39	5727546	0256997	north4		0.5	−0.45	2.64	11.70	59.78	1.47 ± 0.24	47 ± 9
L40	5718323	0251676	west8		1	−0.75	2.39	8.58	55.05		
L41	5716247	0245296	west7		<0.5	−0.20	2.49	11.09	61.87		
L42	5700831	0251158	west1		1	−0.40	2.77	11.65	58.20		
L43	5701758	0250698	west3		0.5	0.25	2.94	14.61	64.87		
L44	5701758	0250698	west3		1	0.35	2.68	14.65	68.29		
L45	5707924	0248529	west6		1	−1.00	2.78	12.55	49.03		

* Elevation refers to the height above the lowest point in the exposure.
\+ F2 = ≥ 4 ϕ (Walker, 1983)
& F1 = ≥ 0ϕ.

3.1.2. Unit 2

The contact between Unit 1 and Unit 2 is sharp (Fig. 3B). Unit 2 is ~1.5 m thick and begins with a 3–12 cm thick basal zone of poorly sorted, cross-stratified, medium to coarse lapilli pyroclasts and lithic ash that pinches and swells across the exposure (Fig. 6). Degassing pipes are prominent on fresh surfaces through this basal layer. The ash layer grades into a massive, very poorly sorted, matrix-supported lapilli tuff. The matrix of this unit is more indurated than Unit 1. The massive section of Unit 2 has a Mdϕ of 0.3, a σ of 2.63, and is reversely graded in the upper 15 cm to a lens of clast-supported coarse lapilli pyroclasts and fine blocks (Fig. 4). Charcoal collected from the clast-supported layer (sample L9) returned a ^{14}C age of 12.643 ± 0.055 thousand years BP (Table 4). Unit 2 componentry includes 77% juvenile pyroclasts and 23% lithics of primarily mafics and lesser amounts of granodiorite and free phenocrysts.

Pyroclasts are subrounded, microvesicular, and contain ≤2% lithic inclusions of mafic lavas and granitic rocks. Like in Unit 1 pyroclasts, the matrix is composed almost entirely of microlites (Fig. 8) but contains only ~3.5% phenocrysts of plagioclase and lesser amounts of olivine, pyroxene, and Fe–Ti oxides. There is little to no glass (Fig. 8B). Pyroclasts exhibit agglomerated textures. Unit 2 has a ϕ_{plag} of 0.42, N_A of 5.08 × 10^4 mm^{-2}, and an N_V of 7.95 × 10^6 mm^{-3} (Table 2). The average plagioclase microlite length is 7 μm. The average density of Unit 2 juveniles is 1.32 ± 0.32 g cm^{-3} with a similar variability of total measured densities (0.62–2.25 g cm^{-3}). Unit 2 has a slightly higher DRE density of 2.78 g cm^{-3}. Pyroclasts have an average vesicularity of 52 ± 12% (Table 1).

Only one sample was measured for Chemistry in Unit 2. This sample has SiO_2, MgO, and FeO contents of 54.28, 3.99, and 11.08 wt%, respectively (Fig. 4; Table 3). The total alkali content is 4.14 wt% while CaO/Al_2O_3 is 0.50 in Unit 2 (Fig. 9). Ba, Ce, and La concentrations increase to 217, 10.15, and 20.99 ppm in Unit 2. In contrast, Sr, Ni, and Cr decrease to 415, 9.15, and 6.07 ppm (Fig. 10, Table 3).

3.1.3. Unit 3

The contact between Unit 2 and Unit 3 is sharp (Fig. 3C and D). Unit 3 is ~4.2 m thick. The lowest 3–5 cm is cross-stratified and similar in appearance to the basal layer of Unit 2. This basal layer grades into a very poorly sorted and indurated massive lapilli tuff. Unit 3 contains ~24% lithics. Unlike other Ci units, Unit 3 lithics are dominated by 48% granite and leucogranite lithics with lesser amounts of mafics and free crystals. The Mdϕ is 0.3 with a σ of 2.71 (Fig. 5, Table 1).

Juvenile pyroclasts are microvesicular, subrounded, have granitic to mafic lithic inclusions, and contain ~3% phenocrysts of plagioclase, olivine, and pyroxene. Similar to other units, pyroclasts are often agglomerates, contain little to no glass, and are composed of >90% microlites of plagioclase, clinopyroxene, olivine, and Fe–Ti oxides. Unit 3 has a ϕ_{plag} of 0.36, N_A of 7.07 × 10^4 mm^{-2}, and an N_V of 1.66 × 10^7 mm^{-3} (Fig. 8C, Table 2). The average measured plagioclase microlite length is 5 μm. Densities vary between 0.63 and 2.69 g cm^{-3} with an average density of 1.39 ± 0.37 g cm^{-3} (Fig. 4). The average vesicularity is 50 ± 13% (Table 1).

The composition of only one sample was measured for chemistry in Unit 3. This sample has the highest SiO_2 content of 54.51 wt% (Fig. 4), lowest MgO content of 3.88 wt%, and the lowest FeO content of 10.98 wt% of all eastern Ci units sampled (Table 3). Total alkalis increase slightly from Unit 2 to 4.20 wt% in Unit 3. The CaO/Al_2O_3 ratio is 0.49. Ba-content increases to 225.47 ppm, while La and Ce both decrease to 9.75 and 20.20 ppm, respectively. Sr slightly decreases further to 414.42 ppm in Unit 3. Ni and Cr both increase from Unit 2 to Unit 3 to 10.05 and 6.17 ppm but are still lower than their Unit 1 averages of 12.25 and 9.36 ppm, respectively (Fig. 10).

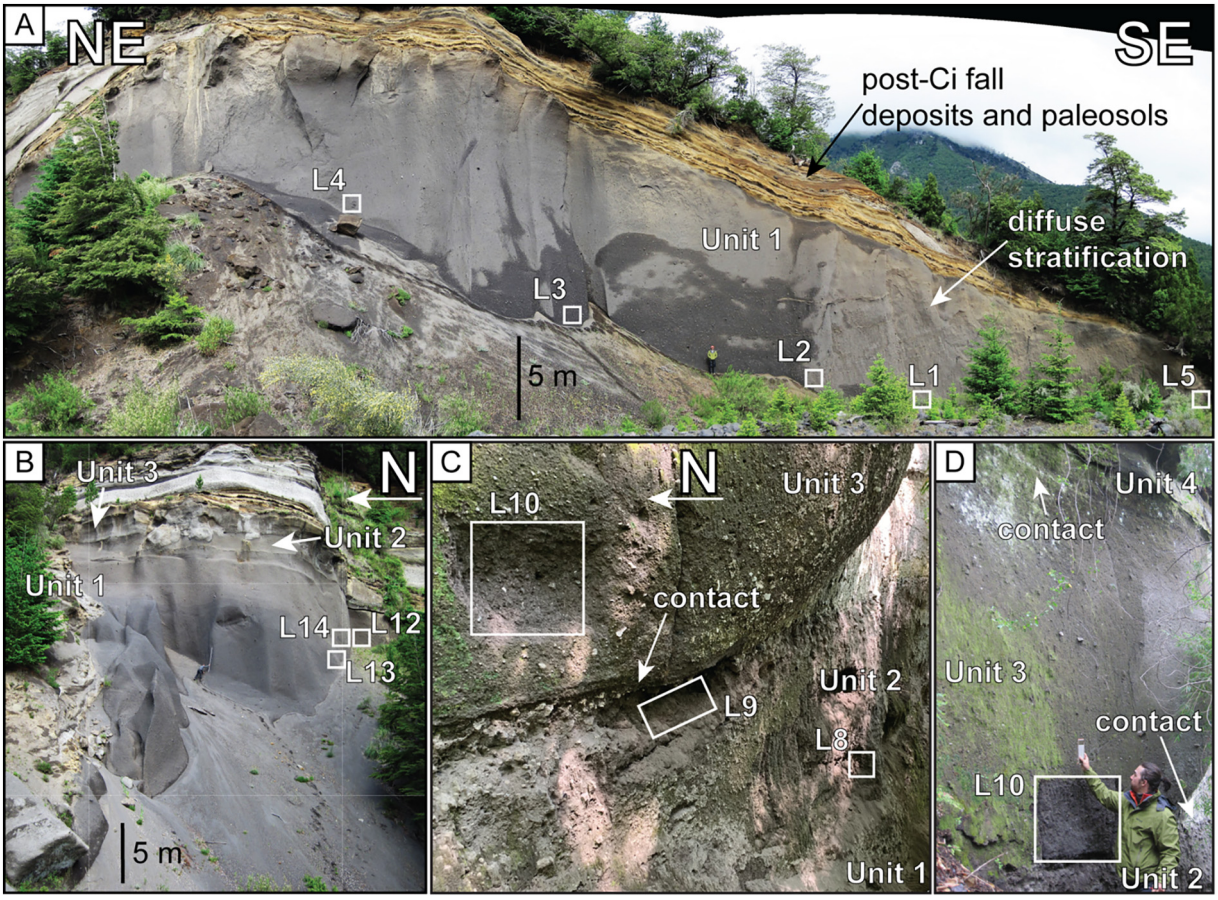

Fig. 3. Outcrop photos from select exposures on the east. We sampled the entire stratigraphy by sampling laterally across three exposures. Sample locations are marked by white boxes. Cardinal directions are in bold white text. (A) Outcrop east1, which is the lowermost part of Unit 1. The base is not exposed. Unit 1 is the thickest flow Unit of the Ci. (B) Outcrop east2 approximately 200 m north of east1. The contact between Unit 1 and Units 2 and 3 is visible but inaccessible. (C) Outcrop east 3 approximately 50 m north of east2. Here we can access the contacts between all flow units. Charcoal collected from Unit 2 (L9) returned an age of 12,643 ± 55 years BP. (D) Outcrop east 3 showing the contact between Units 3 and 4.

3.1.4. Unit 4

The contact between Unit 3 and Unit 4 is sharp (Fig. 3D). Unlike Units 2 and 3, no coarse ash layer exists at the Unit 4 base (Fig. 4). Unit 4 is ~1.1 m thick, massive, very poorly sorted, and indurated. Juvenile content is 74%. Hydrothermally altered lithics make up 51% of lithic material, with lesser amounts of granite, mafics, and free crystals. Unit 4 has a Mdϕ of 0.25 with a σ of 2.25 (Fig. 5, Table 1).

Similar to underlying units, pyroclasts are subrounded, microvesicular, and microlite-rich. Unit 4 has the lowest ϕ_{plag} of 0.29, a N_A of 7.32×10^4 mm^{-2}, and an N_V of 1.84×10^7 mm^{-3} (Table 2). The average measured plagioclase microlite length is 4 μm. Although microlite-rich, Unit 4 has a higher glass content than underlying units (Fig. 8D). Phenocryst content is ≤1%. Juvenile densities are variable between 0.35 and 2.29 g cm^{-3} with an average of 1.41 ± 0.31 g cm^{-3}. Despite Unit 4 having some of the lowest pyroclast densities in the entire eastern stratigraphic section, the average pyroclast density is the densest of all units (Fig. 4). Accordingly, Unit 4's average pyroclast vesicularity of 49 ± 11% is the lowest of all Ci units (Table 1).

Due to the indurated nature of Unit 4 and the difficulty in sampling this unit, we were unable to collect pyroclasts large enough for XRF analysis.

3.2. Select western exposures

3.2.1. West9

West9 is the only location where the base of the Ci is exposed (Fig. 11A inset). The basal contact is with a lava and is sharp. The base contains a high concentration of coarse lapilli and fine blocks, is massive to diffusely stratified and matrix- to clast-supported. Blocks are predominately lithics and include granitic rocks and mafic to intermediate lavas. The exposure is ~25 m thick, dark gray, very poorly sorted, and matrix-supported. There are distinct zones of fine to medium blocks with local concentrations >25% (Fig. 11A). Lithic blocks are predominantly subangular to subrounded and composed of granitic rocks and mafic to intermediate lavas. Similarly, pyroclast blocks are subangular to subrounded, irregularly shaped agglomerates (Fig. 7), and dense. Pyroclasts contain ash- and lapilli-size lithic inclusions of granitic material and mafic lavas. Despite the high block content, these blocky zones are mostly matrix-supported. The matrix is composed of Ci ash similar to the block-poor regions (Fig. 11A) and decrease upsection to <1%. Faint diffuse stratification is evident throughout the exposure. Similar to Units 3 and 4 in the east, this exposure is indurated, but not welded. The exposure is overlain by paleosols and reworked Ci material.

Lapilli-size pyroclasts are subrounded, microvesicular and frothy to dense and glassy, and sometimes exhibit radial jointing or agglomerate textures. Lapilli-size, angular lithic inclusions of granitic material and mafics are common. Sample L23 collected here has a Mdϕ of −1.8 and a σ of 2.30 (Table 1). L23 is compositionally similar with respect to eastern samples (Table 3); with 54.17 wt% SiO_2-content, 3.95 wt% MgO, 10.92 wt% FeO, 4.02 wt% total alkalis, and a CaO/Al_2O_3 ratio of 0.49 (Fig. 9). Cr and Ni are 8.61 and 9.80 ppm, respectively (Fig. 10). Ce is 23.27 ppm, which is slightly higher than eastern exposures. La is 7.72 ppm. Ba is higher than Unit 1 samples at 209 ppm and Sr is 416 ppm.

3.2.2. West 10

West10 is ~1.5 km SW of west9 and in the same drainage (Fig. 2). Unlike west9, the base of west10 is not exposed. Here, the Ci is massive,

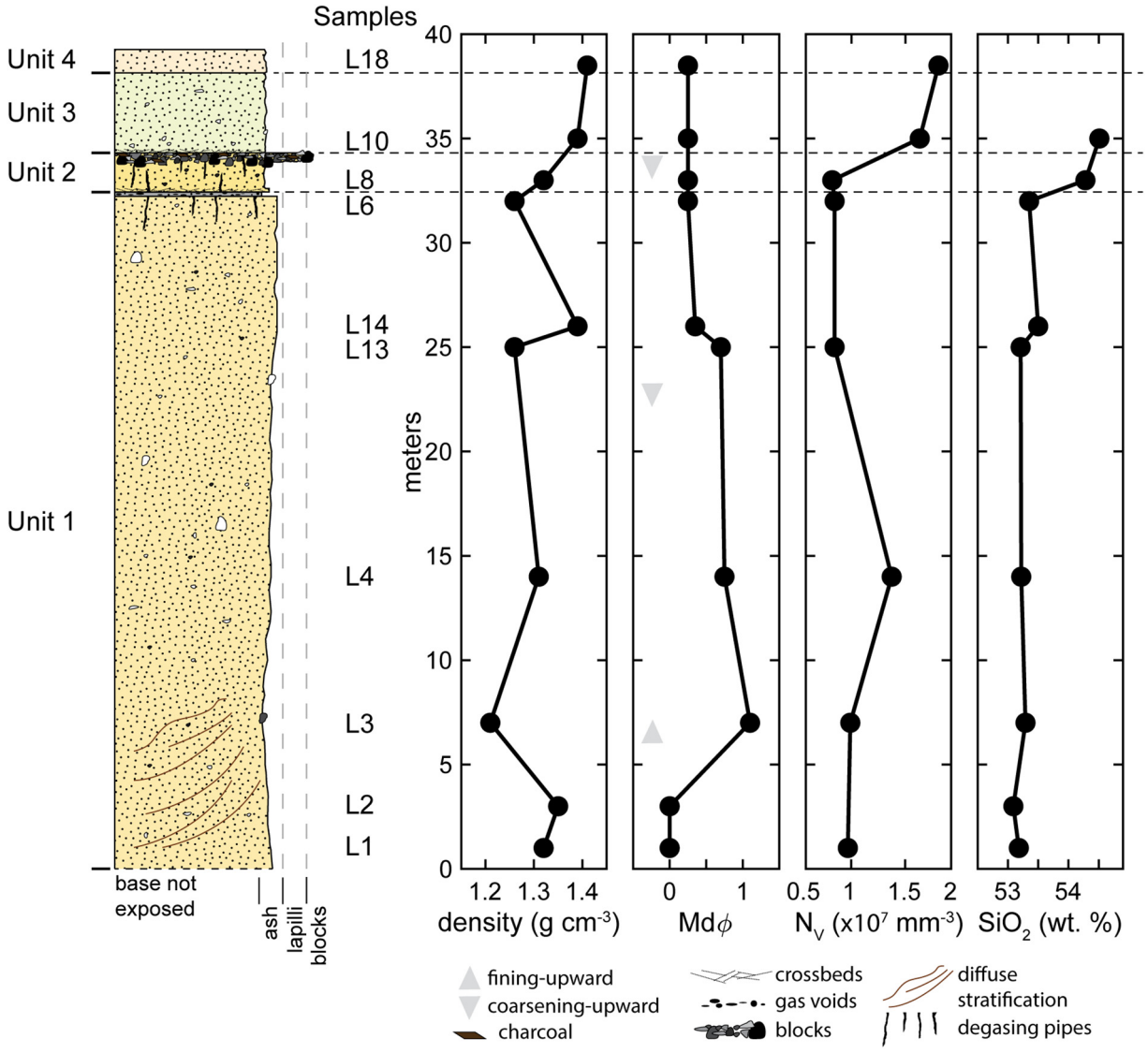

Fig. 4. Stratigraphic column of the eastern Ci stratigraphy across exposures east1, east2, and east3. Plotted alongside the column are the Ci density (g cm^{-3}), Mdϕ, N_V (mm^{-3}), and SiO_2-content to visualize stratigraphic variability. Juvenile densities are highly variable across all units. Unit 1 grain size data fine upwards before slightly coarsening again near the top. Units 2, 3, and 4 have the same Mdϕ. N_V are variable in Unit 1 and steadily increase in overlying units. SiO_2-content is homogenous in Unit 1 and becomes more evolved in Units 2 and 3. Chemistry was not collected for Unit 4.

very poorly sorted, and matrix-supported with little to no diffuse stratification (Fig. 11B). The exposure is ~12 m thick. In sharp contrast to nearby west9, there are little to no large lithic blocks in west10 either as clast-supported lenses or as dispersed material. Instead, blocks are primarily fine-grained in size, juvenile, display agglomerate textures, and have lithic inclusions of granitic material and mafic to intermediate lavas. Sample L24 collected here has a Mdϕ of −2.3 and a σ of 2.29 (Fig. 5, Table 1). Pyroclasts are phenocryst-poor, dense to frothy, and microvesicular, have an average density of 1.45 ± 0.40 g cm^{-3}, and a corresponding vesicularity of 50 ± 0.14%. No chemistry was collected on samples from this site.

3.2.3. West3

Here the Ci is ~1.5 m thick, brown, very poorly sorted, and matrix-supported (Fig. 11C). The base is not exposed and there is minor reworking at the top of the exposure. Blocks and coarse lapilli are locally concentrated, but otherwise the exposure is block-poor. The middle of this exposure has a 1–3 cm thick fine ash lens that both truncates one group of blocks while forming the base of a secondary group of blocks and coarse lapilli (Fig. 11C). The Ci is overlain by reworked material, soils, and vegetation. Samples collected below and above the thin ash layer have a Mdϕ of 0.25 and 0.35 and σ of 2.94 and 2.68, respectively (Table 1). This deposit is a coarse ash tuff that is fines-normal. Charcoal collected from L43 and L44 returned ^{14}C ages of 12.774 ± 0.057 thousand years BP and 12.555 ± 0.055 thousand years BP, respectively (Table 4).

West3 has the most evolved Ci compositions in this study (Table 3), with SiO_2 contents of 57.56 and 57.43 wt% and MgO of 2.44 and 2.51 wt% (Fig. 9). Their FeO content is also low compared to other locations at 9.94 and 9.72 wt%. Accordingly, their total alkali contents of 5.48 and 5.52 wt% are the highest of all samples. Both samples have a CaO/Al_2O_3 ratio of 0.37. L43 and L44 also exhibit elevated Ba, La, Ce compared to other samples, are depleted in Sr with respect to other samples, and have near undetectable and undetectable Cr and Ni content, respectively (Fig. 10). While these major and trace element data are unique in our dataset, they are similar to samples collected by Naranjo and Moreno (2005) and Lohmar (2008); (Fig. 9).

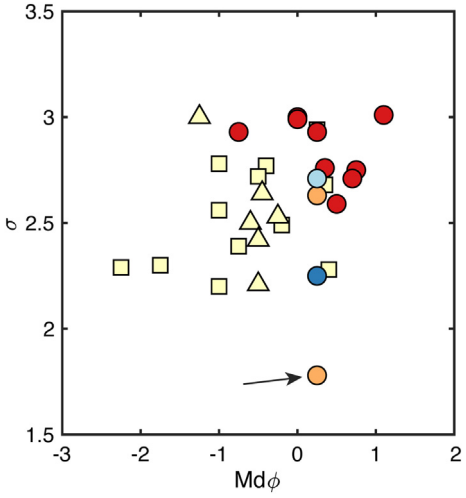

Fig. 5. Ci Mdϕ versus sorting (σ). σ is calculated using the equation of Folk and Ward (1957). Most Ci deposits are very poorly sorted coarse ash tuffs and lapilli tuffs. The arrow points to the cross-bedded basal zone of Unit 2 and is the only poorly sorted sample. Due to a lack of contacts in the north and west, we are unable to differentiate between flow units.

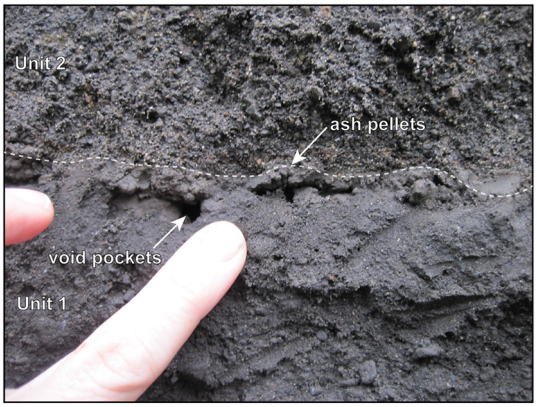

Fig. 6. Contact between Units 1 and 2 at east3–the dashed white line indicates the contact. There are ellipsoidal void pockets in a fine-grained ash capped with ash pellets.

3.3. Select northern exposures

3.3.1. North1

This exposure is ~12 m thick, beige to gray, massive, very poorly sorted, and matrix-supported (Fig. 12A). The base is not exposed and there is surficial reworking at the top of the deposit. The deposits are friable. Minor diffuse stratification is present near the top. The exposure has <1% blocks, but local concentrations can be >10%. Blocks are primarily subangular to subrounded lithics of intermediate lavas and lesser amounts of granitic material. Regions of high block concentration are matrix-supported and not laterally continuous. Juvenile blocks display agglomerate textures, are microporous, and contain lapilli-sized lithic inclusions of intermediate lavas to granitic material. A sharp contact with overlying reworked material and paleosols truncates gas elutriation pipes in the upper 2–3 m. Gas elutriation pipes are evidence throughout the exposure (Fig. 12A).

Pyroclasts are subrounded, microvesicular, and contain lithic inclusions and rare crystal cumulates. Samples were collected at stratigraphic intervals of 1 m, 5 m, and as near to the top as possible (~8 m, Table 1). The Mdϕ at the lowest point is −0.60, fines to −0.25, then coarsens to −0.50. The σ is similarly variable between 2.42 and 2.53. Pyroclast densities decrease upsection from 1.43 ± 0.25 g cm^{-3} to 1.34 ± 0.22 g cm^{-3} at the top. Accordingly, vesicularities increase from 49 ± 9% at the base to 52 ± 8% at the top (Table 1).

The base of north1 has SiO_2 and MgO content of 54.78 and 3.66 wt%, respectively (Table 3). SiO_2 decreases to 50.67 wt% upsection and is the least evolved sample we collected. MgO slightly increases upsection to 3.85 wt%. FeO increases upsection from 10.94 to 12.20 wt% while total alkalis decrease from 4.70 to 3.80 wt%. CaO/Al_2O_3 increases slightly from 0.49 at the base to 0.51 near the top. Ba increases upsection while Sr and Ce decrease. Ni and Cr are low and variable (5.32–9.51 ppm and 5.27–7.57 ppm, respectively).

3.3.2. North2

North2 is 2 m thick, dark gray, massive, very poorly sorted, and matrix supported (Fig. 12C). Like other exposures in the north, the base is not exposed. There are no blocks, visible structures, or depositional features. The top is in sharp contact with overlying paleosols. The exposure contains <1% mafic to intermediate lithics. The Mdϕ is −1.3 with a σ of 3.00 (Table 1). Charcoal collected from this exposure returned a ^{14}C age of 12.696 ± 0.056 thousand years BP (Table 4).

Pyroclasts are subrounded, microvesicular, and contain rare lithic inclusions. Like other exposures, many pyroclasts display agglomerate textures (Fig. 7). The average density is 1.34 ± 0.24 g cm^{-3} and the vesicularity is 52 ± 9% (Table 1). Here, the Ci is compositionally similar to other exposures, with 54.17 wt% SiO_2, 3.66 wt% MgO, 11.05 wt% FeO,

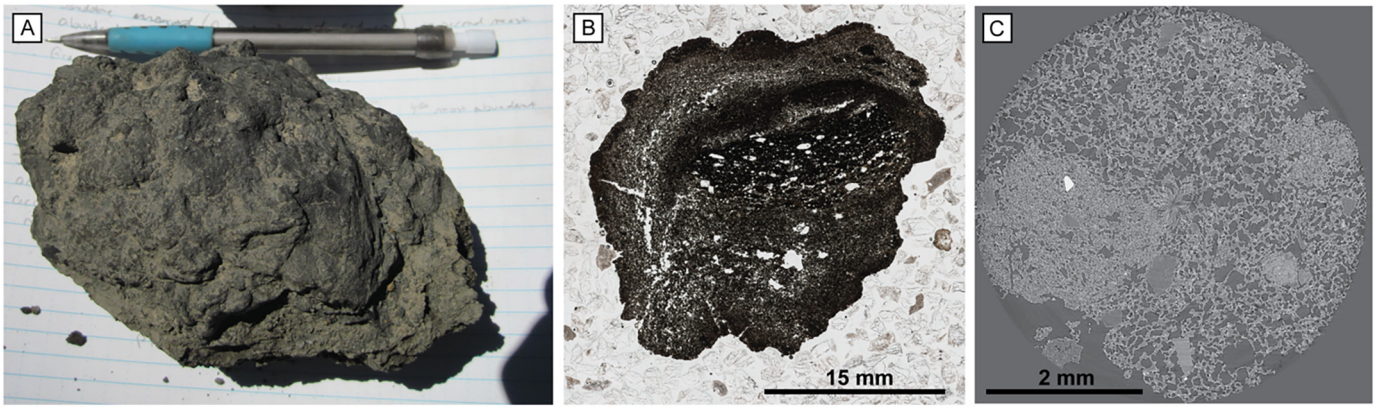

Fig. 7. Examples of clast agglomeration in Ci pyroclasts at multiple scales. (A) Small, agglomerated block from outcrop west9. (B) Thin section scan from outcrop north2. (C) X-ray computed tomography (XRT) slice of a pyroclast from east2 exhibiting small-scale agglomeration. Evidence for clast agglomeration is common in all exposures. See Valdivia et al. (in press) for XRT details.

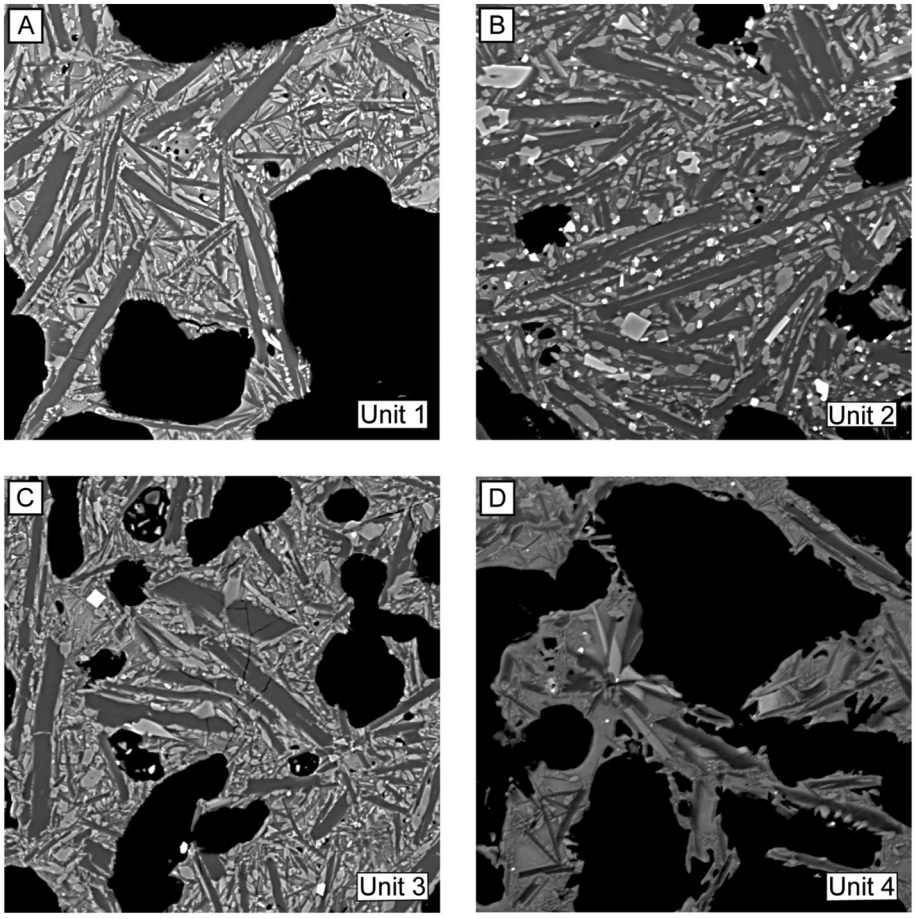

Fig. 8. Backscattered electron images of Ci pyroclasts from flow units in the east. (A) Unit 1; (B) Unit 2; (C) Unit 3; (D) Unit 4. The horizontal field width of each image is 100 μm.

Table 2
Plagioclase microlite textures. All pyroclasts are from the eastern stratigraphic section. Three analyses were conducted for all samples except L3 and L13. The theoretical calculation of mean crystal size S_m from eq. (1) of Blundy and Cashman (2008) is included to show the disagreement between this method and our measured S_m.

Unit	Unit 1					Unit 2	Unit 3	Unit 4
Sample	L1	L3	L4	L13	L6	L8	L10	L18
φ_{plag}	0.39	0.42	0.36	0.42	0.44	0.42	0.36	0.29
S_m (μm)	6.1	5.5	5.1	6.1	6.4	6.5	4.7	4.1
N_A (mm^{-2})	5.56×10^4	5.29×10^4	6.72×10^4	4.99×10^4	5.25×10^4	5.08×10^4	7.07×10^4	7.32×10^4
N_V (mm^{-3})	9.72×10^6	9.55×10^6	1.33×10^7	8.21×10^6	8.21×10^6	7.95×10^6	1.66×10^7	1.84×10^7
S_m (μm)*	2.7	2.8	2.4	2.9	2.9	2.9	2.2	2.0
N_V (mm^{-3})+	2.22×10^7	1.87×10^7	2.89×10^7	1.72×10^7	1.82×10^7	1.78×10^7	3.60×10^7	3.73×10^7
n_{plag}	1113	437	1737	437	985	1307	1796	1180
uncertainty&	3%		2%		3%	3%	2%	3%

* S_m calculated using eq. (1) of Blundy and Cashman (2008).
\+ N_V calculated using the equation for S_m from Blundy and Cashman (2008).
& Calculated using $\frac{\sqrt{n_{plag}}}{n_{plag}}$.

4.66 wt% total alkalis, and a CaO/Al_2O_3 ratio of 0.47 (Table 3). Ni and Cr are low (1.62 and 1.03, respectively) while Ba, Sr, and Ce are similar to other exposures (222, 416, and 22.39 ppm, respectively.

3.3.3. North4

Primary Ci deposits at north4 are up to 3 m thick, dark gray to brown, massive, very poorly sorted, and matrix supported (Fig. 12B). The base is not exposed, and the upper surface of the deposit is reworked. Approximately 10–12 m of reworked Ci material overlies the Ci. The exposure contains <1% blocks. The Mdϕ is −0.5 and the σ is 2.64 (Table 1). Juvenile pyroclasts are subrounded, phenocryst-poor, often agglomerates, and have an average density of 1.47 ± 0.24 g cm^{-3}. Ash- to lapilli-sized lithic inclusions are common. The average vesicularity is 47 ± 9%. Compositions are similar to other north exposures, with 55.33 wt% SiO_2, 3.48 wt% MgO, 10.71 wt% FeO, 4.84 wt% total alkalis, and a CaO/Al_2O_3 ratio of 0.47 (Table 3). At 0.88 and 2.45 ppm, Ni and Cr are lower than nearby north1 and north2. Ba and Ce are the highest in the north (241 and 23.32 ppm, respectively). Sr is 413 ppm and similar to other samples from the north.

4. Discussion

4.1. Correlating deposits regionally

The eastern stratigraphic section is the only location where we identified contacts between individual Ci flow units. Ci deposits in the north and west lack unit contacts, and do not contain discernable granulometric, componentry, or depositional characteristics sufficient to correlate deposits with the four units exposed in the east outcrops.

Compositional similarity of the four eastern flow units and of north and west deposits is also unhelpful for unit correlation. Unit 1 is a basaltic andesite with minimal variability in composition with respect to stratigraphic level. Compositions evolve slightly in Units 2 and 3 (Fig. 4). However, this compositional shift is not a sufficient indicator for unit correlation because the entire XRF dataset compositionally spans from basalt to andesite (Fig. 9). Furthermore, Ci trace element data for Unit 1 are variable and slightly less evolved from Units 2 and 3. The

Table 3
Whole-rock major and trace element geochemistry.

	L1	L2	L3	L4	L13	L14	L12	L6	L8	L10	L16	L23	L43	L44	L34	L35	L36	L37	L39
Unit	Unit 1								Unit 2	Unit 3	Other								
SiO_2	53.18	53.09	53.29	53.22	53.21	53.50	53.58	53.35	54.28	54.51	53.10	54.17	57.56	57.43	54.17	54.78	54.44	50.67	55.33
TiO_2	1.45	1.47	1.47	1.47	1.46	1.46	1.47	1.47	1.46	1.46	1.39	1.46	1.42	1.44	1.51	1.46	1.45	1.54	1.48
Al_2O_3	16.10	16.14	16.18	16.22	16.03	16.05	16.12	16.23	16.13	16.12	16.18	16.17	15.58	15.73	16.12	15.82	15.92	16.88	15.82
FeO*	11.30	11.34	11.32	11.26	11.46	11.30	11.18	11.15	11.08	10.98	10.97	10.92	9.94	9.72	11.05	10.94	11.00	12.20	10.71
MnO	0.18	0.19	0.19	0.19	0.19	0.19	0.19	0.19	0.19	0.19	0.18	0.18	0.29	0.36	0.19	0.19	0.19	0.19	0.19
MgO	4.26	4.26	4.26	4.29	4.22	4.16	4.11	4.30	3.99	3.88	4.11	3.95	2.44	2.51	3.66	3.70	3.85	4.36	3.48
CaO	8.51	8.55	8.52	8.64	8.53	8.45	8.31	8.54	8.05	7.92	8.33	7.97	5.77	5.81	7.58	7.72	7.94	8.67	7.39
Na_2O	3.43	3.50	3.43	3.43	3.65	3.70	3.55	3.52	3.44	3.49	3.39	3.35	4.50	4.55	3.99	3.93	3.81	3.45	4.04
K_2O	0.62	0.61	0.66	0.62	0.64	0.64	0.65	0.62	0.70	0.71	0.63	0.67	0.98	0.97	0.67	0.77	0.73	0.35	0.80
P_2O_5	0.17	0.18	0.18	0.18	0.18	0.18	0.18	0.18	0.19	0.20	0.18	0.19	0.32	0.32	0.22	0.22	0.21	0.13	0.22
Tot.	99.21	99.33	99.48	99.53	99.56	99.63	99.34	99.54	99.52	99.47	98.46	99.01	98.79	98.84	99.16	99.54	99.52	98.44	99.47
Ni	12.41	12.67	12.84	13.96	10.39	10.63	11.43	13.66	9.15	10.05	10.09	9.80	0.00	0.00	1.62	5.32	7.07	9.51	0.88
Cr	9.95	8.32	8.56	10.99	9.36	9.16	8.57	10.00	6.07	6.17	20.34	8.61	0.74	0.74	1.03	5.27	7.57	7.20	2.45
Sc	38.32	38.12	39.60	39.70	37.58	37.88	38.42	39.30	36.52	36.82	37.83	36.63	30.65	30.09	35.04	36.40	36.35	40.87	33.37
V	462.75	464.71	456.51	469.36	463.83	453.05	443.05	461.34	415.51	403.37	394.94	394.52	171.35	178.97	383.72	379.32	399.53	484.90	348.78
Ba	196.90	193.74	201.19	195.33	196.44	201.10	202.52	195.82	216.61	225.47	202.71	208.99	310.02	303.58	221.77	228.67	220.87	203.20	240.84
Rb	12.74	13.00	13.85	12.61	14.02	13.78	12.55	12.03	14.04	15.21	14.59	13.39	21.56	20.27	15.12	15.87	15.69	8.02	17.04
Sr	414.49	415.40	416.31	416.69	419.78	419.29	414.39	413.92	414.52	414.42	419.39	415.50	378.80	381.15	416.21	410.65	412.85	457.42	413.36
Zr	70.62	70.59	73.33	70.29	72.28	73.40	74.47	71.48	78.90	80.99	76.34	79.50	130.36	129.68	86.78	86.19	82.09	74.04	88.54
Y	23.34	23.27	24.48	23.86	23.18	23.18	24.43	22.97	25.27	24.48	24.06	25.74	36.16	36.20	26.31	26.30	25.55	22.39	27.00
Nb	2.27	2.08	2.49	2.28	1.47	1.67	2.56	1.78	2.49	2.69	1.57	2.38	2.90	3.50	2.11	1.82	1.67	1.57	1.81
Ga	19.01	19.50	20.00	20.49	18.91	19.45	19.60	20.10	18.91	20.00	19.06	20.89	21.12	20.54	20.24	18.96	19.40	20.34	19.99
Cu	187.74	201.56	176.51	229.48	134.26	88.25	69.54	124.44	99.50	166.26	171.89	87.22	53.84	61.51	61.54	101.95	94.37	206.58	53.80
Zn	98.70	96.33	97.71	97.81	100.06	96.73	96.33	96.72	100.40	104.77	96.78	98.31	115.79	116.57	104.47	101.16	101.88	102.31	104.27
Pb	6.60	5.64	6.37	6.63	6.86	7.35	8.27	7.62	8.86	9.75	7.45	8.51	11.10	11.48	7.06	8.77	8.45	6.66	7.94
La	6.60	6.63	5.47	3.27	6.96	9.21	8.18	6.83	10.15	9.75	9.31	7.72	16.90	15.56	9.16	11.62	6.97	9.75	11.03
Ce	19.01	14.85	20.40	20.20	20.04	20.43	21.57	16.83	20.99	20.20	19.31	23.27	34.34	40.83	22.39	22.21	21.87	18.28	23.32
Th	0.00	0.59	2.29	1.39	1.42	1.37	1.28	0.79	2.29	1.09	1.32	2.38	2.01	2.22	0.88	1.43	0.29	0.74	1.62
Nd	11.92	11.48	15.52	14.36	13.28	14.26	15.66	11.78	15.02	16.42	13.57	13.86	20.93	20.88	15.09	15.46	13.71	12.25	14.65
U	1.08	2.57	1.29	1.98	2.35	1.67	0.89	0.59	1.59	1.09	1.42	0.50	2.70	1.33	1.32	0.64	1.18	1.57	2.60
Tot.	1594.54	1601.06	1594.70	1650.66	1552.47	1501.86	1473.69	1528.02	1496.79	1569.00	1541.97	1457.70	1361.27	1375.09	1431.86	1478.01	1477.34	1687.59	1413.30

Major elements reported as wt% and trace elements reported as ppm. *FeO = total Fe.

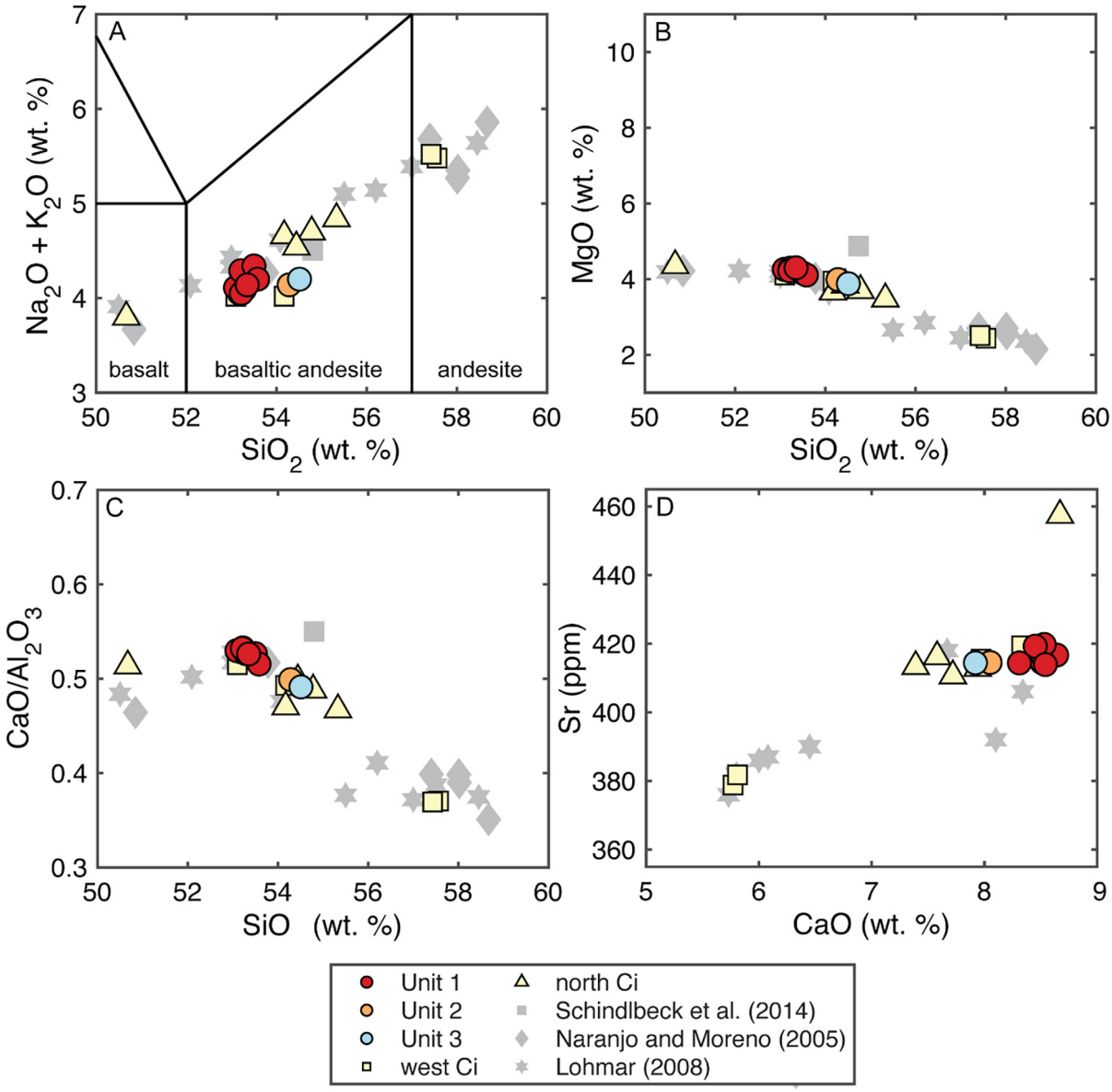

Fig. 9. Whole-rock major element geochemistry. (A) Total alkali-silica diagram. (B) SiO_2 versus MgO Harker diagram. (C) SiO_2 versus CaO/Al_2O_3 Harker diagram. (D) CaO versus Sr diagram. Ci datasets of Naranjo and Moreno (2005), Lohmar (2008), and Schindlbeck et al. (2014) are plotted for comparison. The east stratigraphic section is where we observe the most complete stratigraphy for the Ci. However, the compositional range of the north and west exposures exceeds that of the eastern deposits.

spread of all analyses precludes the use of major and trace element chemistry as flow unit fingerprint regionally (Figs. 9, 10, Table 2), preventing geochemical correlation of units around the volcano. As such, we focus on the eastern stratigraphic section and regional ^{14}C dates to further interpret the Ci emplacement mechanisms and eruption sequence. We recognize that the eastern compositions and granulometry do not represent every Ci exposure. However, because we cannot correlate deposits in the north and west to specific flow units found in the east, and because the eastern stratigraphy has the most complete eruptive sequence, we chose to focus on the eastern stratigraphy to interpret the eruption.

4.2. Interpreting the eruption sequence

The dominant massive coarse ash tuff and massive lapilli tuff characteristics at all outcrops around Llaima suggest deposition from a concentrated pyroclastic density current (PDC) or series of currents (Branney and Kokelaar, 2002). Unit 1 exhibits some diffuse stratification (Fig. 3A), but is mostly massive, poorly sorted, and contains local block concentrations, all of which are common characteristics of valley-ponded PDC deposits. We interpret the massive nature of the deposit and diffuse stratification to represent progressive aggradation from a concentrated pyroclastic current or series of closely spaced currents that resulted in indistinct flow boundaries. Diffuse stratification is likely the result of fluctuations in flow boundary zone shear conditions (Branney and Kokelaar, 2002).

The Unit 1 co-ignimbrite ash suggests a pause in between Unit 1 and Unit 2 deposition long enough to allow settling of the co-ignimbrite ash and pellets (Fig. 6). Ash pellets are indicative of environmental moisture at the time of settling (Van Eaton et al., 2012). Elutriation pipes in the upper 1–2 m of Unit 1 truncate at the co-ignimbrite ash. We interpret the elongated void pockets within the Unit 1 co-ignimbrite ash to represent ponded gas from the Unit 1 elutriation pipes (Fig. 6). This suggests degassing of the Unit 1 ignimbrite occurred following deposition of Unit

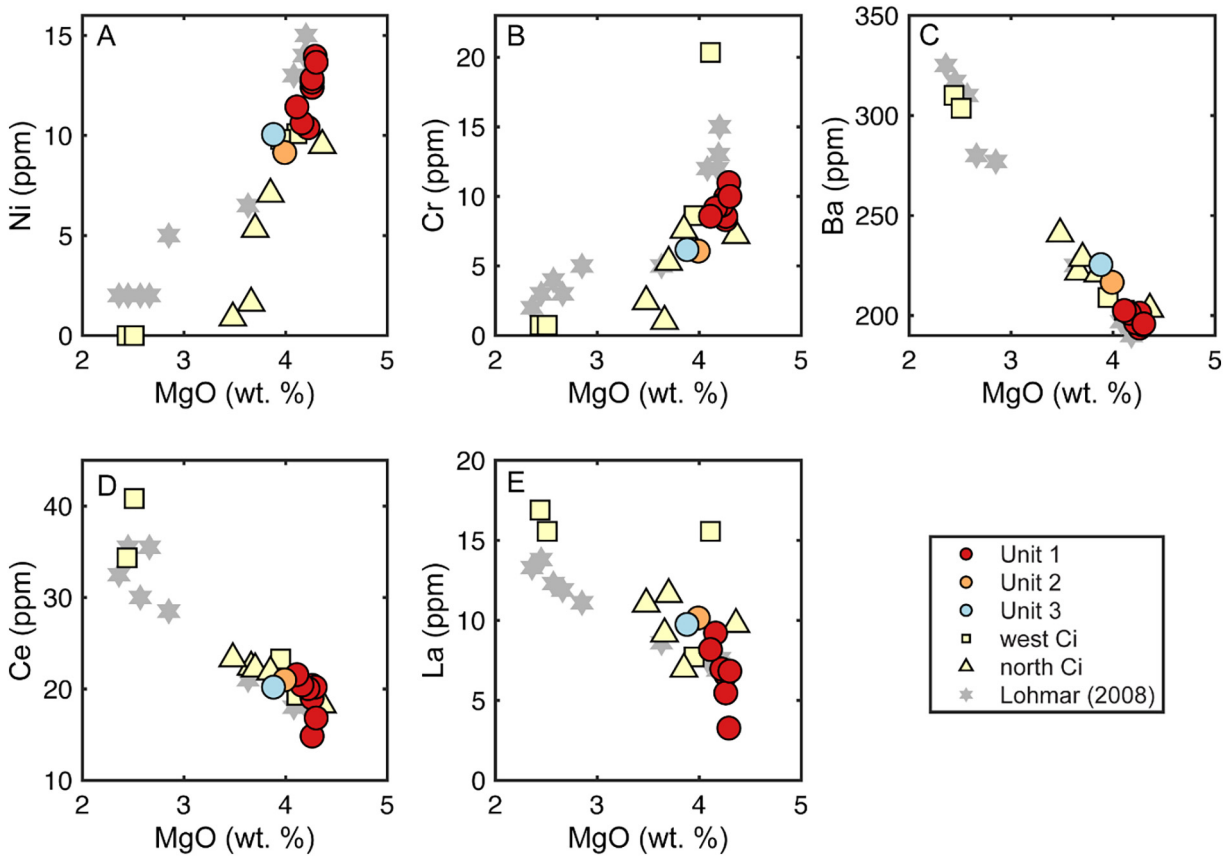

Fig. 10. Select whole-rock Ci trace element geochemistry. (A) MgO versus Ni; (B) MgO versus Cr; (C) MgO versus Ba; (D) MgO versus Ce; (E) MgO versus La.

Table 4
Curacautín ignimbrite radiocarbon analyses. Age reported in years BP. σ is the error. The ^{14}C ages reported in this study are reported as defined by Stuiver and Polach (1977). Naranjo and Moreno (1991) do not report calibration information. Lohmar (2008) ages were calibrated using CALIB 5.0 (Stuiver et al., 2005).

Sample	Latitude	Longitude	^{14}C	σ	Reference
L8	5705558	0271863	12,643	55	this study
L34	5727122	0257641	12,696	56	this study
L42	5700831	0251158	12,754	56	this study
L43	5701758	0250698	12,555	55	this study
L44	5701758	0250698	12,774	57	this study
261,089-2A	5725200	0258800	12,760	130	Naranjo and Moreno (1991)
040487–7	5701900	0251000	13,200	150	Naranjo and Moreno (1991)
190,190-1BC	5705800	0272000	13,260	200	Naranjo and Moreno (1991)
041189–1A	5736200	0253400	13,460	400	Naranjo and Moreno (1991)
LL24B	5709200	0246400	12,510	40	Lohmar (2008)
LL25	5739900	0249900	12,650	140	Lohmar (2008)
LL9-1	5702100	0250900	12,730	90	Lohmar (2008)
LL13	5736200	0253400	13,230	330	Lohmar (2008)

2 with the very low permeability co-ignimbrite ash preventing further gas escape into the overlying deposit. The sharp contact, the preservation of ash pellets and gas pockets, and lack of reworking between Unit 1 and Unit 2 suggest a brief pause in deposition, perhaps no longer than hours to days.

The basal cross-stratified zone of Unit 2 also contains mm-wide, fines-depleted vertical pipes, interpreted as elutriation pipes. This suggests the basal cross-stratified region is a ground layer of the Unit 2 pyroclastic current, likely deposited by a more dilute PDC conditions associated with the current head (e.g., Scarpati et al., 2015); the overlying massive deposit is indicative of deposition by a concentrated PDC. The same interpretation applies for the deposition of Units 3 and 4, although Unit 4 does not have a ground layer. Similar to the contact between Units 1 and 2, the contacts between Units 2 and 3 and Units 3 and 4 are sharp, planar, and continuous with no reworking, incision, or soil horizon development. Therefore, the pauses between Unit 2 and 3 deposition and Unit 3 and 4 deposition are interpreted as similarly short as that between Units 1 and 2 (Fig. 4).

4.3. Is the Ci the result of two eruptions or one?

Naranjo and Moreno (1991) first proposed the Ci as the product of two eruptions separated by ~600 yrs. based on radiocarbon analyses of ~13.2 thousand years BP and ~ 12.6 thousand years BP (Table 4). Lohmar (2008) also adopted the two-eruption model based on their radiocarbon analyses. Naranjo and Moreno (1991) recovered a ^{14}C age of 13,260 ± 200 years BP from the Ci along the Trufulful River in the east that corresponds to our Unit 1. The five radiocarbon dates collected in this study are between 12.774 ± 0.057 and 12.555 ± 0.055 thousand years BP. We did not find any samples in the 13.2–13.8 thousand years BP range (Table 4). We conclude a break of ~600 years between Unit 1 and Unit 2 in the east is not evident, nor is a significant break in deposition evident in any exposure around the volcano. Based on the extent of our ^{14}C sampling area combined with our new radiocarbon ages, we suggest a single eruptive episode at ~12.6 thousand years BP produced the entire Ci.

4.4. Volume estimate

To reassess the Ci volume, we use the deposit extent in our study, the deposit extent mapped in the earlier work of Naranjo and Moreno (2005), and a range of maximum slopes of deposition to refine the volume calculation. Hill slopes of max Ci deposition are between 0° and 62.5° with an average of 8.9 ± 8.7° (1σ). Approximately 46% of all points

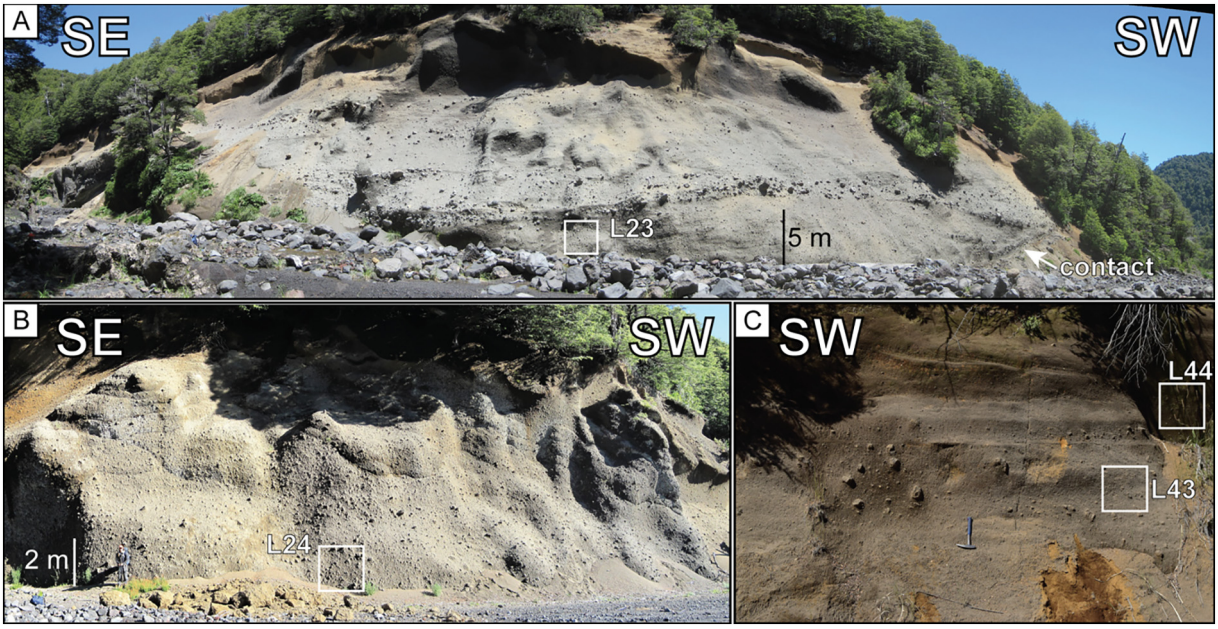

Fig. 11. Select Ci exposures in the west. Sample locations are shown in white boxes. Cardinal directions are in bold white text. (A) Outcrop west9 is an ~25 m thick, indurated exposure where the base is exposed (white arrow). West9 has the highest concentration of blocks of any exposures in this study. The zones of blocks are matrix-supported, and the matrix is composed of Curacautín ash. (B) Outcrop west10 ~ 2 km southwest of west9 and located downstream in the same drainage. The base is not exposed here and the high concentration of blocks disappears. (C) Outcrop west3 where we collected ^{14}C ages of 12.774 ± 0.057 thousand years BP (L43) and 12.555 ± 0.055 thousand years BP (L44).

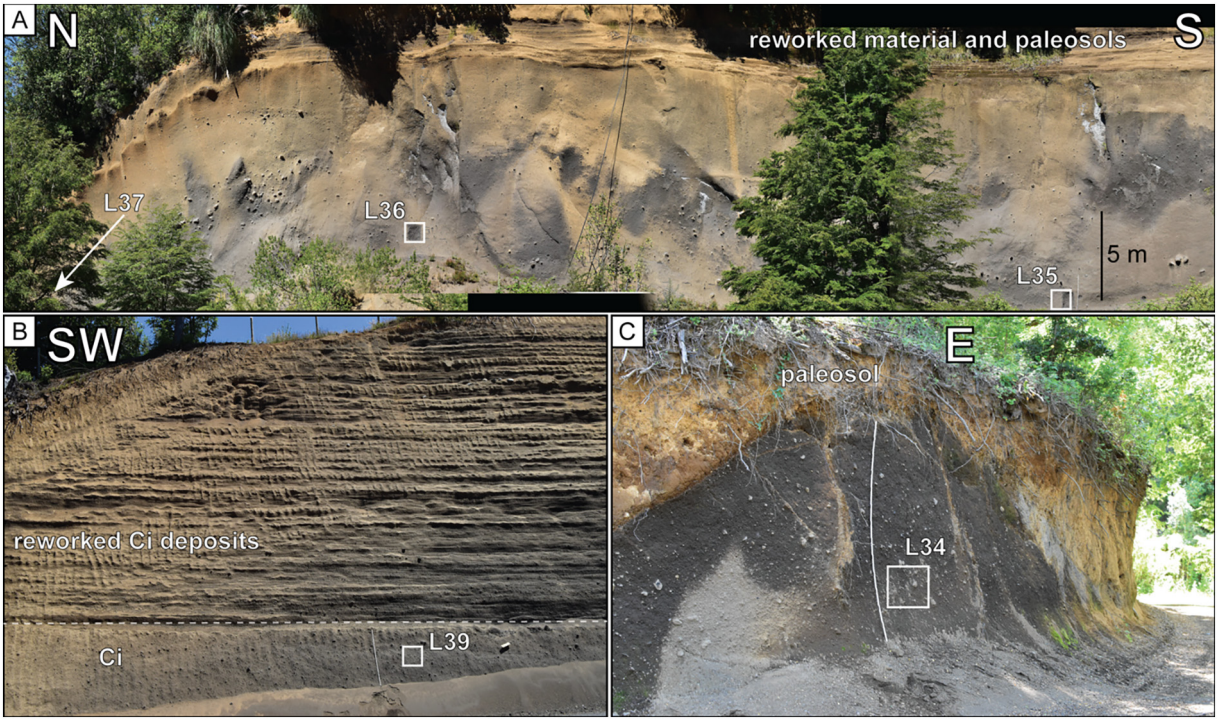

Fig. 12. Select Ci exposures in the north. Sample locations are shown in white boxes. Cardinal directions are in bold white text. (A) North1 is the thickest exposure in the north. (B) Exposure north4 exhibiting extensive reworking of Ci material. White scale is 2 m. The dashed line marks the contact between the Ci and reworked Ci. (C) Exposure north2. Charcoal collected here returned a ^{14}C age of 12.696 ± 0.056 thousand years BP.

(8033) are shallower than 5° and 71% are below 10° (12,424). These data are similar to the Campanian (Silleni et al., 2020) and Taupo (Wilson and Walker, 1985) ignimbrites. We use 0-m isopachs of 9° (average), 13.5° (+0.5σ), and 17.5° (+1σ) to estimate three volumes for the Ci (Fig. 13). We estimate multiple 0-m isopachs to quantify the sensitivity of our estimate with respect to the depositional slope.

The areas encompassed by the 9°, 13.5°, and 17.5° 0-m isopachs are 896 km^2, 963 km^2, and 981 km^2, respectively (Fig. 14). Integrating the region under the area versus thickness curves yields tephra volume estimates of 7.60 km^3, 8.33 km^3, and 8.58 km^3. Using an average vesicularity of 52%, the calculated DRE volumes are 3.95 km^3, 4.33 km^3, and 4.46 km^3.

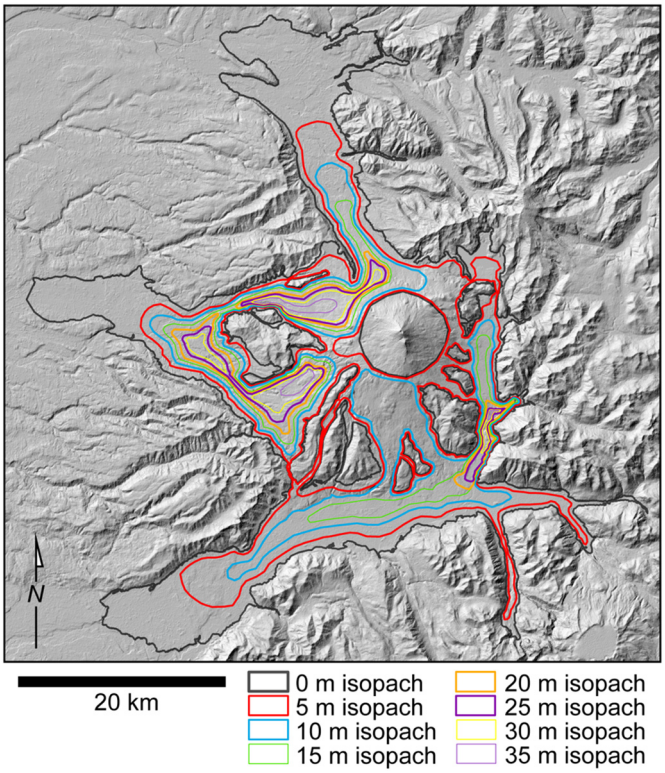

Fig. 13. Isopach map of the Ci volume estimate with a 0-m isopach of 9°. Isopachs are drawn based on measured stratigraphic sections of this study and Lohmar (2008), field observations, and extrapolation of observations and slope data. An 8 km wide region representing a caldera as hypothesized by Naranjo and Moreno (1991) was removed from the volume estimate.

We calculated a fourth volume estimate using the 13.5° slope and encompassing a region approximate to that of Naranjo and Moreno (1991) (Fig. 1). An 8 km diameter circular area was removed to represent a caldera as hypothesized by Naranjo and Moreno (1991). The area of this estimate is 1625 km^2. Using the same 52% vesicularity, the calculated tephra volume is 10.02 km^3 and the DRE is 5.21 km^3.

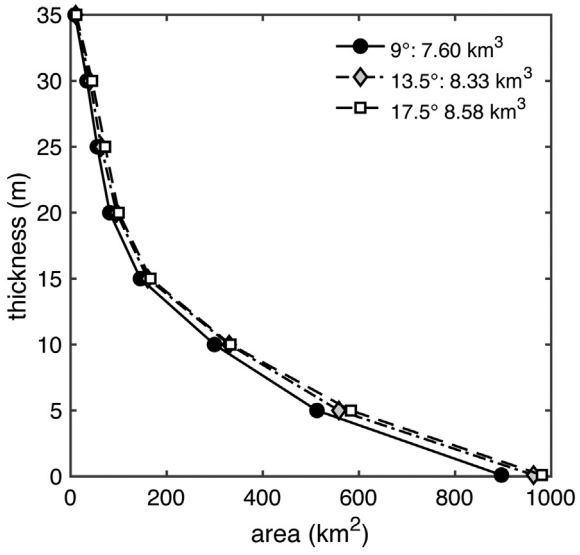

Fig. 14. The Ci volume estimate in this study based on the isopach tracing method. The tephra volume is the integration of the area under the curve.

Naranjo and Moreno (1991) map the Ci up to 100 km west of Llaima (Fig. 1), but do not provide location data for exposures. During our mapping we did not locate any exposures >30 km from Llaima. Additionally, the base of the Ci is only exposed at one location in this study (Fig. 10A). Our volume estimates are based on outer-caldera deposits only. No fall deposits for the Curacautín eruption have ever been found. Therefore, the volume estimates herein should be considered minimum estimates. Because our 9° average maximum slope of deposition is similar to that of Wilson and Walker (1985) and Silleni et al. (2020), the tephra volume estimate of 7.60 km^3, or 3.95 km^3 DRE is most reasonable.

Our reported volume estimates have the following limitations. Because we did not have borehole data in the region, we could not approximate Ci thickness in areas where no surface exposures exist. Additionally, because we were not able to locate Ci deposits beyond ~30 km, we were limited in how far we could reasonably approximate runout. We restricted our isopachs to 5 m rather than more precise isopachs such as 1 m due to our limited data, which includes stratigraphic sections of this study and those of Lohmar (2008). Finally, because we only found the base of the Ci in one exposure, our deposit thinning estimate is a minimum, and our volume estimate should only be considered a first order approximation.

4.5. What were the magmatic conditions that drove the eruption?

The two most likely mechanisms to generate highly explosive mafic eruptions are rapid magma ascent rates combined with fast crystallization during ascent (e.g., Arzilli et al., 2019; Bamber et al., 2020) and magma-water interaction (e.g., Ross and White, 2005). Rapid ascent rates generate high degrees of undercooling and disequilibrium that can induce extensive and rapid microlite crystallization, thus increasing magma viscosity and trapping magmatic volatiles necessary for brittle fragmentation. Conversely, magma-water interaction involves the efficient transfer and release of thermal energy from a magma to a water source which drives explosivity (Zimanowski et al., 2015). Distinguishing between magmatic or phreatomagmatic fragmentation involves scrutiny of deposit characteristics and pyroclast textures. For example, pyroclasts of well-documented mafic explosive eruptions attributed to rapid magma ascent have characteristically high microlite contents that are evidence of high undercooling (Sable et al., 2006; Sable et al., 2009; Vinkler et al., 2012; Bamber et al., 2020); the deposits of magma-water interaction have high proportions of fines (>4ϕ) due to high fragmentation efficiency, and blocky ash grains (e.g., Walker, 1981; De Rita et al., 2002). Below we offer an interpretation for the primary fragmentation mechanism that drove the Ci eruption based on field observations and laboratory analyses.

Unlike the deposits of phreatomagmatic eruptions, Ci exposures are mostly homogenous and lack any depositional features common to wet eruptions such as soft sediment deformation, low-angle cross strata, palagonite, and sideromelane (Figs. 3, 11, 12). Agglomerate clasts are common in Ci exposures (Fig. 7) and suggestive of temperatures higher than those observed in phreatomagmatic eruptions. Ash pellets preserved within the Unit 1 thin co-ignimbrite ash (Fig. 6) are conspicuous but may well be a product of atmospheric moisture rather than magma-water interaction (White and Valentine, 2016). In addition, the Mdϕ and fines content of the Ci (average Mdϕ of −0.27 and an average σ of 2.60; Table 1) are not consistent with similar mafic ignimbrites associated with magma-water interaction. Specifically, the Ci contains 73% moderately vesiculated ash on average, with only 13.2–19.8% total mass being fine ash, although we do note that Unit 1 is slightly fines-enriched. This is in contrast to the more typical 85–95% low vesicularity ash found in mafic ignimbrite-forming eruptions driven by magma-water interaction (e.g., Heiken and Wohletz, 1985; De Rita et al., 2002; Giordano et al., 2002; Miyabuchi et al., 2006).

We also investigated ash grains using scanning electron microscopy to look for surface features consistent with magma-water interaction (blocky grains, surface fractures, and adhering dust; Heiken and

Wohletz, 1985; Büttner et al., 1999; Miyabuchi et al., 2006). Many ash particles are blocky to vesicular, but we do not see cracking or fine ash adhered to surfaces. Componentry analysis of Ci ash reveals a high relative proportion of scoria to lithics (22–29%), which indicates a lower amount of conduit margin breakage in the subsurface. We do note that approximately 51% of Unit 4 lithics are hydrothermally altered, which may suggest the latter stage of the Ci eruption interacted with some form of external water similar to the waning stages of the 122 Etna (Sable et al., 2006) and Tarawera 1886 (Houghton et al., 2004) eruptions. However, the high concentration of hydrothermally altered lithics may alternatively be a result of the conduit excavating a hydrothermally altered region of Llaima and not an influence of external water.

The only evidence that magma-water interaction may have played a role are the pervasive inclusions of country rock within pyroclasts. Inclusions are dominated by mafic lavas, and thus are likely excavated from Llaima's ancestral shield volcano lavas within 500–1000 m of the surface, where we might expect there to be groundwater (depth based on geologic map, Naranjo and Moreno, 2005). Indeed, wall rock brecciation is common in phreatomagmatic eruptions (see White and Ross, 2011); thus, phreatic activity or magma-water interaction along the conduit margins is a plausible explanation for the brecciation and injection of wall rock into the ascending magma. However, the agglomerate textures suggest clast fusing in the conduit post injection of wall rock, which is unexpected in phreatomagmatic eruptions due to the rapid lowering of temperatures. Therefore, our observations of Ci grain size, ash textures, componentry, inclusion of wall rock material within pyroclasts, and evidence for ash fusing suggest that, while magma-water interaction may have played some role in the eruption, it was not the driving mechanism that led to the Ci explosive conditions. Instead, we turn to the microlites for evidence of the conditions that promoted strong explosivity.

The interplay of bubbles and crystals during magma ascent has a considerable influence on eruption style. Microlites are particularly important as they can both facilitate degassing by creating new sites for bubble nucleation or suppress gas escape by increasing bulk viscosity and bubble network tortuosity (Vona et al., 2011; Moitra et al., 2018; Arzilli et al., 2019). For example, Sparks (1978) found that a critical vesicularity of ~75% for magmatic fragmentation in crystal-free magmas. In contrast, Arzilli et al. (2019) show the requirements for Plinian basaltic eruptions are temperatures <1100 °C, *syn*-eruptive crystal contents of more than 30%, and a bulk viscosity of 10^5 Pa s. Experiments by Lindo et al. (2017) show that the vesicularity of permeability onset in basaltic andesites is reached at vesicularities ≤56% when crystallization is greater than ~20%. This implies that at 20% crystallization, permeability is enhanced, and thus gas escape through a permeable magma could be a prevailing process. However, this was clearly not the case for the Curacautín magma

Many microlite morphologies observed in Ci pyroclasts, such as acicular, swallowtail, and skeletal, are associated with disequilibrium crystallization conditions and hence rapid growth (Hammer and Rutherford, 2002; Szramek et al., 2006; Shea and Hammer, 2013). Plagioclase microlite fractions in Ci pyroclasts (Fig. 8) are 0.29–0.44 (Table 2), well above the ~20% total crystallinity necessary to drop vesicularity of permeability onset to ≤56%. Plagioclase ϕ_{plag} and N_A textures are consistent with nucleation-dominated crystallization (Blundy and Cashman, 2008) and are suggestive of rapid magma ascent (Fig. 15). An analysis of plagioclase crystal size distributions (CSDs) suggests the population and size distribution of Ci plagioclase formed in seconds to hours, further supporting a rapid ascent hypothesis (Valdivia Muñoz et al., 2021).

Ci vesicularities are between 43 ± 10% and 71 ± 10% and, as such, are within the critical vesicularity range for magmatic fragmentation of a crystal-bearing melt (Arzilli et al., 2019) (Fig. 4). Our microlite and vesicularity data are therefore most consistent with those observed in brittle fragmentation of a basaltic andesite magma. Further, Valdivia

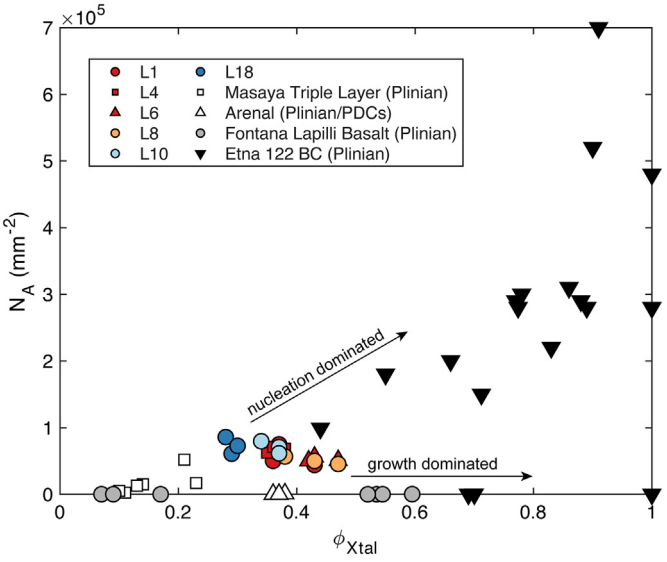

Fig. 15. Crystal fraction (ϕ_{Xtal}) versus area number density N_A (mm^{-2}) for the Ci (this study), Masaya Triple Layer (Bamber et al., 2020), Etna 122 BCE (Sable et al., 2006), mafic Plinian and PDC deposits of Arenal volcano (Szramek et al., 2006), and the Fontana Lapilli Basalt (Costantini et al., 2010). Costantini et al. (2010) report a range of values for ϕ_{Xtal} and the median of those ranges are plotted here. Only plagioclase ϕ and N_A are reported for the Ci. Other notable mafic explosive eruptions include the 1886 eruption of Tarawera volcano, New Zealand. Pyroclasts of that eruption contain 85–99% microlites, dominated by 57% plagioclase, 40% clinopyroxene, 2% olivine, and < 1% FeTi oxides (Sable et al., 2009). The 2001 hydromagmatic to Strombolian and ash explosions eruption of Etna volcano produced N_A from 10^3 to 10^5 mm^{-2} and glass contents of 12.6–76.1% (Taddeucci et al., 2004). An interesting observation is that high N_A, while typically associated with mafic explosive activity, is not always a necessity of high explosivity mafic eruptions. High N_A are typically attributed to undercooling from rapid ascent that drives disequilibrium crystallization (Arzilli et al., 2019), but these data highlight that such conditions are not always preserved in the pyroclast record. However, Ci plagioclase number densities are consistent with nucleation-dominated crystallization (Blundy and Cashman, 2008), a process attributed to high undercooling.

Muñoz et al. (2021) found that 99% of the Ci vesicle network is interconnected but convoluted with high values of tortuosity. Additionally, they show that permeabilities of Ci pyroclasts calculated from 3D X-ray computed microtomography analyses are 0.3–6.3 × 10^{-12} m^2. These permeabilities are slightly lower than those of other basaltic explosive eruptions (Colombier et al., 2021), and suggest that even though permeability was established, the Curacautín magma was unable to efficiently lose gas, resulting in a coupling of the gas to the magma. Using the bubble number density meter of Toramaru (2006), Valdivia Muñoz et al. (2021) estimated a decompression rate for the Curacautín magma of 1.4 MPa s^{-1}. This rate is similar to the rates of 1.5 and 2.0 MPa s^{-1} calculated for the 1886 Tarawera and Etna 122 BCE eruptions, respectively Shea (2017). Additionally, Valdivia Muñoz et al. (2021) calculated a minimum overpressure of 5 MPa necessary to fragment the Curacautín magma, suggesting that rapid ascent could have generated the overpressure needed to fragment the microlite-bearing magma.

Comparing the Ci magmatic conditions to similar eruptions lends further insight into the conditions that produce explosive basaltic volcanism. The critical vesicularity of 30% necessary for brittle fragmentation of mafic magmas assumes crystallization must occur for mafic explosive volcanism (Arzilli et al., 2019). However, there are examples of mafic systems that erupt explosively but produce relatively glassy pyroclasts (e.g., Costantini et al., 2010; Bamber et al., 2020). The Fontana lapilli basalt is interpreted to be the result of rapid decompression, but not attributed to microlite crystallization and a subsequent rheological shift in the magma (Costantini et al., 2010). Instead, that eruption appears to be the result of phreatomagmatism and late decompression-induced homogeneous bubble nucleation from rapid ascent. Eruption temperatures are estimated at 1100 °C, which are likely too hot for extensive microlite crystallization by the time of eruption.

Therefore, the rapid quenching from magma-water interaction and high temperatures are expected to produce relatively glass-rich pyroclasts (Fig. 15). Similarly, the Masaya Triple Layer eruption (Bamber et al., 2020) contains both microlite-rich and microlite-poor pyroclasts but have a 50–80% glass matrix (Fig. 15). However, Masaya microlite N_V are at most only one order of magnitude different from those measured in the Ci and are comparable to N_V calculated in other explosive mafic eruptions (e.g., Etna, Tarawera; Sable et al., 2006; Sable et al., 2009). Additionally, Masaya microlite S_m are approximately half the size of those measured for the Ci. This may suggest that crystallization of the Ci magma began deeper in the conduit and would explain why Masaya has a high N_V but still high glass content. The deviation between our microlite calculations and those of similar eruptions may results from a range of microlite shapes and sizes that nevertheless produce a similar rheological shift to enable brittle behavior.

Our proposed model of rapid ascent of a partially degassed basaltic andesite magma contrasts with recent work by Ruth et al. (2016) that posits that the 2008 Strombolian activity at Llaima is the result of repeated injection of mafic magma batches, crystal mush remobilization, and extensive vesiculation. They calculated depths of magma storage between 1 and 4 km with recharge magmas rising from 14 km depth. Schindlbeck et al. (2014) calculated depths of Ci storage at ~18 km. Rapid ascent from greater depths would result in higher degrees of undercooling as the magma nears the surface, resulting in a faster rheological shift that locked up the Ci magma and inhibited degassing (Valdivia Muñoz et al., 2021). The 2008 Strombolian eruption, by comparison, was passively degassing from a semi-shallow crystal mush zone that upon repeated addition of deeper magmas, unlocked trapped gases that triggered rapid ascent and subsequent Strombolian activity. We speculate that Llaima's varying degrees of explosivity may reflect ranges in the depths from which the erupted magmas originated, suggesting that the size of magma injection may have an important control on the intensity of explosivity from Llaima.

To summarize, lithic entrainment within pyroclasts and the presence of hydrothermally altered accidentals suggest magma-water interaction may have played some role in the Curacautín eruption. However, the microlite textures, vesicle network properties, and evidence for pyroclast fusing in the conduit suggest that undercooling-induced crystallization, resulting from rapid magma ascent, resulted in both an increase in the Ci bulk magma viscosity and coupling of the gas to the magma, allowing the magma to reach the threshold necessary for brittle fragmentation of a crystal-bearing melt. Though we have not experimentally quantified the Ci ascent rate here, plagioclase microlite textures are on the order of magnitude of similar mafic explosive eruptions (Sable et al., 2006; Sable et al., 2009; Vinkler et al., 2012; Bamber et al., 2020).

4.6. Conceptual eruption model

The observed high microlite crystallinity, disequilibrium microlite morphologies, and moderate vesicularities are consistent with magmatic fragmentation of a rapidly ascending and partially degassed melt (Lindo et al., 2017; Moitra et al., 2018; Arzilli et al., 2019). Polylobate bubbles shaped by the high microlite content suggest bubble nucleation and degassing occurred due to a combination of rapid decompression and new nucleation sites created during microlite crystallization. The resulting increase in viscosity and bubble overpressure would likely have been sufficient to fragment the bulk magma brittlely.

Juvenile pyroclast vesicularities, bubble textures, and microlite textures are similar between Units 1, 2, and 3, suggesting similar conditions in ascent rate and fragmentation mechanisms. Unit 4, the thinnest of the Ci Units, has lower vesicularities and higher bulk densities relative to underlying units (Fig. 4). Unit 4 also has the lowest plagioclase microlite content, suggesting a decrease in decompression rate that allowed the ascending magma to maintain a lesser degree of undercooling or supersaturation, enabling enhanced degassing. This unit likely represents the waning stage of the eruption.

The Curacautín eruption paused for hours to days at the end of Unit 1, which allowed a fine-grained co-ignimbrite ash to deposit. Atmospheric moisture likely promoted the formation of massive ash pellets that cap the co-ignimbrite ash. Due to the lack of fine-grained laminae coating the ash pellets, they were likely deposited after the passing of the ash-rich Unit 1 pyroclastic current wake, thus not accreting fine ash to form accretionary lapilli (Brown et al., 2010). Degassing of Unit 1 generated gas elutriation pipes in the upper 1–2 m and circular to elongated gas pockets (void spaces; Fig. 6) within co-ignimbrite ash of Unit I. We interpret that most of Unit 1 degassing occurred following the deposition of Unit 2, whereby the coignimbrite ash acted as a low permeability layer that trapped escaping gas from Unit 1. The sharp contacts, lack of reworking, evidence for primary ignimbrite deposits (e.g., elutriation pipes), and planar contacts between Units 1, 2, and 3 suggest a short-lived pause between deposition of ignimbrites. Unlike Unit 1, there are no ash pellets or a fine ash cap overlying Unit 2 or 3, suggesting subsequent currents deposited before co-ignimbrite ash could settle.

Different componentry for Units 2 and 3 may indicate a shift in vent location or fragmentation depth. For example, a higher concentration of granitic basement material in Unit 3 than Units 1, 2, and 4 could indicate fragmentation of bedrock deeper in the conduit or migration of the vent. The higher population of hydrothermally altered lithics in Unit 4 may indicate some interaction with external water or hydrothermally altered country rock.

Our minimum tephra volume estimate of 6.79–7.60 km^3 (Fig. 14) corresponds to a VEI5 Plinian eruption (Newhall and Self, 1982). There is no evidence that significant additional volume was deposited as a co-ignimbrite ash following the cessation of the eruption. The common image invoked by Plinian eruptions is a convecting column of ash and bombs towering tens of km into the atmosphere. The Ci, however, lacks any fall deposits and is composed entirely of valley-filling tuffs. Further, all Ci exposures contain agglomerate pyroclasts (Fig. 7), which suggest clasts were interacting with and impacting one another in the conduit before deposition. These observations suggest the Ci eruption was a boiling over event or collapsing low column that infilled valleys and drainages around Llaima with the deposits of concentrated pyroclastic currents (e.g., Giordano and Dobran, 1994; Giordano and Doronzo, 2017; Smith et al., 2020).

Trolese et al. (2019) show that total collapse regimes that generate long runout PDCs (>20 km) result from a high amount of collapsing mass at low collapse heights. Due to their inability to entrain atmospheric air and cool down, these eruptions tend to be hot and result in deposit welding (Trolese et al., 2019). As noted above, the Ci lacks fall deposits, which we interpret to represent a collapse regime or boiling over event. However, the Ci is entirely nonwelded. The lack of welding is most likely due to the microlite rich and glass poor nature of the pyroclasts.

Based on our volume estimates, the Curacautín eruption cleared 1.1–1.2×10^{13} kg of material from Llaima's reservoir. Modeling by Carey and Sigurdsson (1989) found that minimum mass eruption rates of 2.0×10^8 kg s^{-1} are associated with large-volume pyroclastic current generation. Using our estimated erupted mass of 1.09–1.24×10^{13} kg and a minimum eruption rate for pyroclastic current generation of 2.0×10^8 kg s^{-1}, we estimate a Curacautín eruption duration of ~15–17 h. We note that mass eruption rates are heavily dependent on parameters such as vent radius, shape, and eruption temperature (Trolese et al., 2019), and therefore these eruption durations are only first order approximations.

4.7. The caldera hypothesis

Naranjo and Moreno (1991) hypothesize the Ci eruption formed an 8-km diameter caldera due to the volume of material evacuated from the chamber and that Holocene deposits cover this caldera. Barometric

measurements by Schindlbeck et al. (2014) place the Ci melt residence at ~18 km depth corresponding to a roof aspect ratio (R) of ~2.25, where R is the ratio of reservoir depth to reservoir diameter. Roche and Druitt (2001) show that R values <1 are consistent with coherent caldera collapse while R values >1.4 are associated with incoherent caldera collapse. R values >2 may indicate caldera formation from incoherent faulting between the reservoir and surface, but Roche and Druitt (2001) stress this is not always the case because upward propagating faults may intersect at depth and cease their upward migration. One such case is the 1600 CE eruption of Huaynaputina, during which ~11 km^3 of DRE magma was erupted from reservoirs at ~20 km and ~ 6 km, and a volumetrically equivalent caldera did not form (Lavallée et al., 2006). Therefore, we conclude there is not sufficient evidence corroborating the caldera-collapse hypothesis. Geophysical surveys capable of resolving subvolcanic features at depths of 20 km may be necessary to further explore the caldera model (Davy and Caldwell, 1998).

5. Conclusions

The Ci is an impressive example of the explosive endmember of mafic volcanism. We conducted extensive field and petrographic studies to develop a new conceptual eruption model for the Ci. Our field observations, including no evidence for a significant time break between flow units, and new ^{14}C data suggest the Curacautín eruption was a single event at ~12.6–12.7 thousand years BP. All juvenile clasts exhibit extensive microlite crystallization, polylobate vesicle networks, and moderate vesicularities that suggest this eruption was triggered by brittle magmatic fragmentation of a rapidly ascending, non-degassed, and highly viscous (relative to typical basaltic andesite magmas) bulk magma. Using new detailed field observations and stratigraphic sections of Lohmar (2008) and this study, we estimate the minimum Ci tephra volume between 7.6 and 8.6 km^3 (DRE volume of 4.0–4.5 km^3) and a total mass of 1.1-1.2 $\times 10^{13}$ kg. Our volume estimate and single eruption model allow us to estimate an eruption duration of ~15–17 h. Despite the large volume, we did not find sufficient evidence to suggest the Curacautín eruption generated a volumetrically equivalent caldera. Our case study of the Ci supports a growing body of literature that suggests rapid ascent rates are one of the primary drivers for strongly explosive mafic eruptions (Houghton et al., 2004; Sable et al., 2006; Sable et al., 2009; Moitra et al., 2018; Arzilli et al., 2019; Bamber et al., 2020).

Future work is necessary to further constrain the conditions that promoted the explosive Ci eruption. The lack of fall deposits is peculiar and may be explained by an investigation of vent geometry. Further textural investigation of agglomerate textures and lithic inclusions are important for constraining processes within the conduit (e.g., magma-water interaction). More detailed whole-rock, trace element, and isotope studies are necessary to better resolve pre-eruptive conditions for the Ci. Comparison of Ci pyroclast textures with those created using high pressure-temperature decompression experiments of Ci melts could quantify decompression paths and the degree of Ci melt undercooling and plagioclase supersaturation (Shea and Hammer, 2013). Magma rheology experiments (e.g., Vona et al., 2011) could constrain the viscoelastic evolution of the Ci melt related to different temperatures and degrees of undercooling and would complement the decompression experiments with respect to textural comparison. Both the decompression experiments and rheology experiments could serve to extend numerical models of microlite nucleation and growth developed for silicic magmas (e.g., Andrews and Befus, 2020) to mafic compositions, providing additional quantitative insights into crystallization kinetics in mafic systems such as Llaima volcano.

Declaration of Competing Interest

There are no competing commercial or financial relationships that present a conflict of interest with the work published in this manuscript.

Acknowledgements

Funding was provided by National Geographic Society grant 9942-16, National Science Foundation EAR grant 1831143, a Boise State University Department of Geosciences Burnham Grant, and a Smithsonian Institution Pre-Doctoral Fellowship awarded to AM. AM thanks Constanza Perales Moya for their help during the 2019 field campaign, Aurora Silleni and Caroline Bouvet de Maissoneuve for their helpful conversations, and Tom Giachetti for running samples on the He-pycnometer at the University of Oregon. Thoughtful reviews by Fabio Arzilli, one anonymous reviewer, and editor Jim Gardner greatly improved the clarity and content of this manuscript.

References

Andrews, B.J., Befus, K.S., 2020. Supersaturation Nucleation and growth of Plagioclase: a numerical model of decompression-induced crystallization. Contrib. Mineral. Petrol. 175, 23. https://doi.org/10.1007/s00410-020-1660-9.

Arzilli, F., La Spina, G., Burton, M.R., Polacci, M., Le Gall, N., Hartley, M.E., Di Genova, D., Cai, B., Vo, N.T., Bamber, E.C., Nonni, S., Atwood, R., Llewellin, E.W., Brooker, R.A., Mader, H. M., Lee, P.D., 2019. Magma fragmentation in highly explosive basaltic eruptions induced by rapid crystallization. Nat. Geosci. 12, 1023–1028. https://doi.org/10.1038/s41561-019-0468-6.

Baker, D.R., Mancini, L., Polacci, M., Higgins, M.D., Gualda, G.A.R., Hill, R.J., Rivers, M.L., 2012a. An introduction to the application of X-ray microtomography to the three-dimensional study of igneous rocks. Lithos 148, 262–276. https://doi.org/10.1016/j.lithos.2012.06.008.

Baker, D.R., Brun, F., O'Shaughnessy, C., Mancini, L., Fife, J.L., Rivers, M., 2012b. A four-dimensional X-ray tomographic microscopy study of bubble growth in basaltic foam. Nat. Commun. 3, 1135. https://doi.org/10.1038/ncomms2134.

Bamber, E.C., Arzilli, F., Polacci, M., Hartley, M.E., Fellowes, J., Di Genova, D., Chavarría, D., Saballos, J.A., Burton, M.R., 2020. Pre- and *syn*-eruptive conditions of a basaltic Plinian eruption at Masaya Volcano, Nicaragua: the Masaya Triple Layer (2.1 ka). J. Volcanol. Geotherm. Res. 392, 1–16. https://doi.org/10.1016/j.jvolgeores.2019.106761.

Befus, K.S., Andrews, B.J., 2018. Crystal nucleation and growth produced by continuous decompression of Pinatubo magma. Contrib. Mineral. Petrol. 173, 92. https://doi.org/10.1007/s00410-018-1519-5.

Blundy, J., Cashman, K.V., 2008. Petrologic reconstruction of magmatic system variables and processes *in:* Minerals, Inclusions and Volcanic Processes. Rev. Mineral. Geochem. 69, 179–239.

Branney, M.J., Kokelaar, P., 2002. Pyroclastic density currents and the sedimentation of ignimbrites. Geol. Soc. Lond. Mem. 27, 1. https://doi.org/10.1144/GSL.MEM.2003.027.

Brown, R.J., Branney, M.J., Maher, C., Dávila-Harris, P., 2010. Origin of accretionary lapilli with ground-hugging density currents: evidence from pyroclastic couplets on Tenerife. Geol. Soc. Am. Bull. 122, 305–320. https://doi.org/10.1130/B26449.1.

Büttner, R., Dellino, P., Zimanowski, B., 1999. Identifying magma-water interaction from the surface features of ash particles. Nature 401, 688–690.

Carey, S., Sigurdsson, H., 1989. The intensity of Plinian eruptions. Bull. Volcanol. 51, 28–40.

Carey, R.J., Manga, M., Degruyter, W., Gonnermann, H., Swanson, D., Houghton, B., Orr, T., Patrick, M., 2013. Convection in a volcanic conduit recorded by bubbles. Geology 41, 395–398. https://doi.org/10.1130/G33685.1.

Cashman, K.V., Giordano, G., 2014. Calderas and magma reservoirs. J. Volcanol. Geotherm. Res. 288, 28–45. https://doi.org/10.1016/j.jvolgeores.2014.09.007.

Cembrano, J., Lara, L., 2009. The link between volcanism and tectonics in the southern volcanic zone of the Chilean Andes: a review. Tectonophysics 471, 96–113. https://doi.org/10.1016/j.tecto.2009.02.038.

Colombier, M., Vasseur, J., Houghton, B.F., Cáceres, F., Scheu, B., Kueppers, U., Dingwell, D. B., 2021. Degassing and gas percolation in basaltic magmas. Earth Planet. Sci. Lett. 573, 117134. https://doi.org/10.1016/j.epsl.2021.117134.

Coltelli, M., Del Carlo, P., Vezzoli, L., 1998. Discovery of a Plinian basaltic eruption of Roman age at Etna volcano, Italy. Geology 26, 1095–1098.

Costantini, L., Bonadonna, C., Houghton, B.F., Wehrmann, H., 2009. New physical characterization of the Fontana Lapilli basaltic Plinian eruption, Nicaragua. Bull. Volcanol. 71, 337–355. https://doi.org/10.1007/s00445-008-0227-9.

Costantini, L., Houghton, B.F., Bonadonna, C., 2010. Constraints on eruption dynamics of basaltic explosive activity derived from chemical and microtextural study: The example of the Fontana Lapilli Plinian eruption, Nicaragua. J. Volcanol. Geotherm. Res. 189, 207–224.

Couch, S., 2003. Experimental investigation of crystallization kinetics in a haplogranite system. Am. Mineral. 88, 1471–1485.

Davy, B.W., Caldwell, T.G., 1998. Gravity, magnetic and seismic surveys of the caldera complex, Lake Taupo, North Island, New Zealand. J. Volcanol. Geotherm. Res. 81, 69–89.

De Rita, D., Giordano, G., Esposito, A., Fabbri, M., Rodani, S., 2002. Large volume phreatomagmatic ignimbrites from the Colli Albani volcano (Middle Pleistocene, Italy). J. Volcanol. Geotherm. Res. 118, 77–98.

Degruyter, W., Burgisser, A., Bachmann, O., Malaspinas, O., 2010. Synchrotron X-ray microtomography and lattice Boltzmann simulations of gas flow through volcanic pumices. Geosphere 6, 470–481. https://doi.org/10.1130/GES00555.1.

Di Genova, D., Brooker, R.A., Mader, H.M., Drewitt, J.W.E., Longo, A., Deubener, J., Neuville, D.R., Fanara, S., Shebanova, O., Anzellini, S., Arzilli, F., Bamber, E.C., Hennet, L., La Spina,

G., Miyajima, N., 2020. In situ observation of nanolite growth in volcanic melt: a driving force for explosive eruptions. Sci. Adv. 6. https://doi.org/10.1126/sciadv.abb0413.
Dzierma, Y., Wehrmann, H., 2010. Eruption time series statistically examined: Probabilities of future eruptions at Villarrica and Llaima Volcanoes, Southern Volcanic Zone, Chile. J. Volcanol. Geotherm. Res. 193, 82–92. https://doi.org/10.1016/j.jvolgeores.2010.03.009.
Folk, R.L., Ward, W.C., 1957. Brazos River Bar: a Study in the significance of grain size Parameters. J. Sediment. Petrol. 27 (1), 3–26.
Franco, L., Palma, J.L., Lara, L.E., Gil-Cruz, F., Cardona, C., Basulato, D., Martín, J.S., 2019. Eruptive sequence and seismic activity of Llaima volcano (Chile) during the 2007–2009 eruptive period: Inferences of the magmatic feeding system. J. Volcanol. Geotherm. Res. 379, 90–105.
Freda, C., Gaeta, M., Giaccio, B., Marra, F., Palladino, D.M., Scarlato, P., Sottilli, G., 2011. CO_2-driven large mafic explosive eruptions: the Pozzolane Rosse case study from the Colli Albani Volcanic District (Italy). Bull. Volcanol. 73 (3), 241–256. https://doi.org/10.1007/s00445-010-0406-3.
Giachetti, T., Burgisser, A., Arbaret, L., Druitt, T.H., Kelfoun, K., 2011. Quantitative textural analysis of Vulcanian pyroclasts (Montserrat) using multi-scale X-ray computed microtomography: comparison with results from 2D image analysis. Bull. Volcanol. 73, 1295–1309. https://doi.org/10.1007/s00445-011-0472-1.
Giordano, G., Dobran, F., 1994. Computer simulations of the Tuscolano Artemisio's second pyroclastic flow unit (Alban Hills, Latium, Italy). J. Volcanol. Geotherm. Res. 61 (1–2), 69–94.
Giordano, G., Doronzo, D.M., 2017. Sedimentation and mobility of PDCs: a reappraisal of ignimbrites' aspect ratio. Sci. Rep. 7 (1), 1–7. https://doi.org/10.1038/s41598-017-04880-6.
Giordano, G., De Rita, D., Cas, R., Rodani, S., 2002. Valley pond and ignimbrite veneer deposits in the small-volume phreatomagmatic 'Peperino Albano' basic ignimbrite, Lago Albano maar, Colli Albani volcano, Italy: influence of topography. J. Volcanol. Geotherm. Res. 118, 131–144.
Giordano, G., De Benedetti, A.A., Diana, A., Dino, G., Gaudioso, F., Marasco, F., Miceli, M., Mollo, S., Cas, R.A.F., Funiciello, R., 2006. The Colli Albani mafic caldera (Rome, Italy): stratigrapahy, structure and petrology. J. Volcanol. Geotherm. Res. 155, 49–80. https://doi.org/10.1016/j.jvolgeores.2006.02.009.
Hammer, J.E., Rutherford, M.J., 2002. An experimental study of the kinetics of decompression-induced crystallization in silicic melt. J. Geophys. Res. 107, B1. https://doi.org/10.1029/2001JB000281.
Hammer, J.E., Cashman, K.V., Hoblitt, R.P., Newman, S., 1999. Degassing and microlite crystallization during pre-climatic events of the 1991 eruption of Mt. Pinatubo, Philippines. Bull. Volcanol. 60, 355–380.
Heiken, G., Wohletz, K.H., 1985. Volcanic Ash. University of California press, Berkeley 246 p.
Hogg, A.G., Hua, Q., Blackwell, P.G., Niu, M., Buck, C.E., Guilderson, T.P., Heaton, T.J., Palmer, J.G., Reimer, P.J., Reimer, R.W., Turney, C.S.M., Zimmerman, S.R.H., 2013. SHCal13 Southern Hemisphere Calibration, 0-50,000 years cal BP. Radiocarbon 55 (4), 1889–1903. https://doi.org/10.2458/azu_js_rc.55.16783.
Houghton, B.F., Gonnermann, H.M., 2008. Basaltic explosive volcanism: constraints from deposits and models. Chem. Erde 68, 117–140.
Houghton, B.F., Wilson, C.J.N., 1989. A vesicularity index for pyroclastic deposits. Bull. Volcanol. 51, 451–462.
Houghton, B.F., Wilson, C.J.N., Del Carlo, P., Coltelli, M., Sable, J.E., Carey, R., 2004. The influence of conduit processes on changes in styles of basaltic Plinian eruptions: Tarawera 1886 and Etna 122 BC. J. Volcanol. Geotherm. Res. 137, 1–14.
Johnson, D.M., Hooper, P.R., Conrey, R.M., 1999. XRF analysis of rocks and minerals for major and trace elements on a single low dilution li-tetraborate fused bead. Adv. X-ray Anal. 41, 843–867.
La Spina, G., Burton, M., de Michieli Vitturi, M., Arzilli, F., 2016. Role of syn-eruptive plagioclase disequilibrium crystallization in basaltic magma ascent dynamics. Nat. Commun. 7, 13402. https://doi.org/10.1038/ncomms13402.
Lavallée, Y., de Silva, S.L., Salas, G., Byrnes, J.M., 2006. Explosive volcanism (VEI 6) without caldera formation: insight from Huaynaputina volcano, southern Peru. Bull. Volcanol. 68, 333–348. https://doi.org/10.1007/s00445-005-0010-0.
Lindo, A., Larsen, J.F., Chasmna, K.V., Oppenheimer, J., 2017. Crystal controls on permeability development and degassing in basaltic andesite magma. Geology 45, 831–834. https://doi.org/10.1130/G39157.1.
Lohmar, S., 2008. Petrologia de las ignimbritas Lican y Pucon (volcan Villarrica) y Curacautin (volcan Llaima) en los Andes del sur de Chile. DissertationUniversity of Chile.
Lohmar, S., Parada, M.A., Robin, C., Gerbe, M.C., Deniel, C., Gourgaud, A., Lopez-Escobar, L., Moreno, H., Naranjo, J.A., 2006. Origin of Postglacial 'Mafic' Ignimbrites at Llaima and Villarrica Volcanoes (Southern Andes, Chile): Assimilation of Plutonic Rocks as One of the Triggering Factors? Abstract, Simposio Sudamericano de Geología Isotópica (SSAGI). Punta del Este, Chile.
Lohmar, S., Robin, C., Gourgaud, A., Clavero, J., Parada, M.A., Moreno, H., Ersoy, O., Lopez-Escobar, L., Naranjo, J.A., 2007. Evidence of magma-water interaction during the 13,800 years BP explosive cycle of the Licán Ignimbrite, Villarrica volcano (southern Chile). Rev. Geol. Chile 34, 233–247.
Martí, J., Planagumà, L.I., Geyer, A., Aguirre-Díaz, G., Pedrazzi, D., Bolós, X., 2017. Basaltic ignimbrites in monogenetic volcanism: the example of La Garrotxa volcanic field. Bull. Volcanol. 79 (33). https://doi.org/10.1007/s00445-017-1113-0.
Miyabuchi, Y., Watanabe, K., Egawa, Y., 2006. Bomb-rich basaltic pyroclastic flow deposit from Nakadake, Aso Volcano, southwestern Japan. J. Volcanol. Geotherm. Res. 155, 90–103. https://doi.org/10.1016/j.jvolgeorest.2006.02.007.
Miyaji, N., Kan'no, A., Kanamaru, T., Mannen, K., 2011. High-resolution reconstruction of the Hoei eruption (AD 1707) of Fuji volcano, Japan. J. Volcanol. Geotherm. Res. 207, 113–129. https://doi.org/10.1016/j.jvolgeores.2011.06.013.
Moitra, P., Gonnermann, H.M., Houghton, B.F., Tiwary, C.S., 2018. Fragmentation and Plinian eruption of crystallizing basaltic magma. Earth Planet. Sci. Lett. 500, 97–104. https://doi.org/10.1016/j.epsl.2018.08.003.
Naranjo, J.A., Moreno, H., 1991. Actividad explosiva postglacial en el volcan Llaima, Andes del sur. Rev. Geol. Chile 18, 69–80.
Naranjo, J.A., Moreno, H., 2005. Geología del volcán Llaima, region de la Araucanía. Carta Geol. Chile Scale 88, 1–33.
Newhall, C.G., Self, S., 1982. The Volcanic Explosivity Index (VEI): an Estimate of Explosive Magnitude for Historical Volcanism. J. Geophys. Res. 87, 1231–1238.
Papale, P., 1999. Strain-induced magma fragmentation in explosive eruptions. Nature 397, 425–428. https://doi.org/10.1038/17109.
Parfitt, E., 2004. A discussion of the mechanisms of explosive basaltic eruptions. J. Volcanol. Geotherm. Res. 134, 77–107. https://doi.org/10.1016/j.jvolgeores.2004.01.002.
Pérez, W., Freundt, A., Kutterolf, S., 2020. The basaltic plininan eruption of the ~6 ka San Antonio Tephra and formation of the Masaya caldera, Nicaragua. J. Volcanol. Geotherm. Res. 401, 1–17. https://doi.org/10.1016/j.jvolgeores.2020.106975.
Roche, O., Druitt, T.H., 2001. Onset of caldera collapse during ignimbrite eruptions. Earth Planet. Sci. Lett. 191, 191–202.
Ross, P.-S., White, J.D.L., 2005. Mafic, large-volume, pyroclastic density current deposits from phreatomagmatic eruptions in the Ferrar large igneous province, Antarctica. Geology 113, 627–649. https://doi.org/10.1086/449324.
Ruth, D.C.S., Cottrell, E., Cortés, J.A., Kelley, K.A., Calder, E.S., 2016. From Passive Degassing to Violent Strombolian Eruption: the Case of the 2008 Eruption of Llaima Volcano, Chile. J. Petrol. 57, 1833–1864. https://doi.org/10.1093/petrology/egw063.
Sable, J., Houghton, B., Del Carlo, P., Coltelli, M., 2006. Changing conditions of magma ascent and fragmentation during the Etna 122 BC basaltic Plinian eruption: evidence from clast microtextures. J. Volcanol. Geotherm. Res. 158, 433–456. https://doi.org/10.1016/j.jvolgeores.2006.07.006.
Sable, J.E., Houghton, B.F., Wilson, C.J.N., Carey, R.J., 2009. Eruption mechanisms during the climax of the Tarawera 1886 basaltic Plinian eruption inferred from microtextural characteristics of the deposits. In: Thordarson, T., Self, S., Larsen, G., Rowland, S.K., Hoskuldsson, A. (Eds.), Studies in Volcanology: the Legacy of George Walker. vol. 2. The Geological Society of London, London, pp. 229–254 Special Publications of IAVCEI.
Scarpati, C., Sparice, D., Perrotta, A., 2015. The ground layer of the Campanian Ignimbrite: an example of deposition from a dilute pyroclastic density current. Bull. Volcanol. 77 (11), 1–10. https://doi.org/10.1007/s00445-015-0985-0.
Schindlbeck, J.C., Freundt, A., Kutterolf, S., 2014. Major changes in the post-glacial evolution of magmatic compositions and pre-eruptive conditions at Llaima volcano, Andean Southern Volcanic Zone, Chile. Bull. Volcanol. 76, 830. https://doi.org/10.1007/s00445-014-0830-x.
Schneider, C.A., Rasband, W.S., Eliceiri, K.W., 2012. NIH image to ImageJ: 25 years of image analysis. Nat. Methods 9, 671–675.
Shea, T., 2017. Bubble nucleation in magmas: a dominantly heterogeneous process? J. Volcanol. Geotherm. Res. 343, 155–170. https://doi.org/10.1016/j.jvolgeores.2017.06.025.
Shea, T., Hammer, J.E., 2013. Kinetics of cooling- and decompression-induced crystallization in hydrous mafic-intermediate magmas. J. Volcanol. Geotherm. Res. 260, 127–145. https://doi.org/10.1016/j.jvolgeores.2013.04.018.
Shea, T., Houghton, B.F., Gurioli, L., Cashman, K.V., Hammer, J.E., Hobden, B.J., 2010. Textural studies of vesicles in volcanic rocks: an integrated methodology. J. Volcanol. Geotherm. Res. 190, 271–289. https://doi.org/10.1016/j.jvolgeores.2009.12.003.
Silleni, A., Giordano, G., Isaia, R., Ort, M.H., 2020. Magnitude of the 39.8 ka Campanian Ignimbrite Eruption, Italy: a review and reassessment using an ignimbrite isopach map. Front. Earth Sci. https://doi.org/10.3389/feart.2020.543399.
Smith, G., Rowley, P., Williams, R., Giordano, G., Trolese, M., Silleni, A., Parsons, D.R., Capon, S., 2020. A bedform phase diagram for dense granular currents. Nat. Commun. 11 (1), 1–11. https://doi.org/10.1038/s41467-020-16657-z.
Sparks R.S.J., 1978. The dynamics of bubble formation and growth in magmas: a review and analysis. J Volcanol Geotherm Res 3 (1–2), 1–37. https://doi.org/10.1016/0377-0273(78)90002-1.
Stern, C.R., 2004. Active Andean volcanism: its geologic and tectonic setting. Rev. Geol. Chile 31, 161–206.
Stuiver, M., Polach, H.A., 1977. Reporting of ^{14}C Data. Radiocarbon 19 (3), 355–363.
Stuiver, M., Reimer, P.J., Reimer, R.W., 2005. CALIB 5.0. http://calib.org/calib/.
Szramek, L., 2016. Mafic Plinian eruptions: is fast ascent required? J. Geophys. Res. B Solid Earth 121, 7119–7136. https://doi.org/10.1002/2016JB013208.
Szramek, L., Gardner, J.E., Larsen, 2006. Degassing and microlite crystallization of basaltic andesite magma erupting at Arenal Volcano, Costa Rica. J. Volcanol. Geotherm. Res. 157, 182–201. https://doi.org/10.1016/j.jvolgeores.2006.03.039.
Taddeucci, J., Pompilio, M., Scarlato, P., 2004. Conduit processes during the July–August 2001 explosive activity of Mt. Etna (Italy): inferences from glass chemistry and crystal size distribution of ash particles. J. Volcanol. Geotherm. Res. 137, 33–54. https://doi.org/10.1016/j.jvolgeores.2004.05.011.
Toramaru, A., 2006. BND (bubble number density) decompression rate meter for explosive volcanic eruptions. J. Volcanol. Geotherm. Res. 154, 303–316. https://doi.org/10.1016/j.jvolgeores.2006.03.027.
Trolese, M., Cerminara, M., Ongaro, T.E., Giordano, G., 2019. The footprint of column collapse regimes on pyroclastic flow temperatures and plume heights. Nat. Commun. 10, 2476. https://doi.org/10.1038/s41467-019-10337-3.
Valdivia Muñoz, P.A., Marshall, A.A., Brand, B.D., Manga, M., Huber, C., 2021. Mafic explosive volcanism at Llaima volcano: 3D X-ray microtomography reconstruction of pyroclasts to constrain shallow conduit processes. Bull. Volcanol. https://doi.org/10.1007/s00445-021-01514-8 (*in revision*).

Van Eaton, A.R., Muirhead, J.D., Wilson, C.J.N., Cimarelli, C., 2012. Growth of volcanic ash aggregates in the presence of liquid water and ice: an experimental approach. Bull. Volcanol. 74, 1963–1984. https://doi.org/10.1007/s00445-012-0634-9.

Vinkler, A.P., Cashman, K., Giordano, G., Groppelli, G., 2012. Evolution of the mafic Villa Senni caldera-forming eruption at Colli Albani volcano, Italy, indicated by textural analysis of juvenile fragments. J. Volcanol. Geotherm. Res. 235–236, 37–54. https://doi.org/10.1016/j.jvolgeores.2012.03.006.

Völker, D., Kutterolf, S., Wehrmann, H., 2011. Comparative mass balance of volcanic edifices at the southern volcanic zone of the Andes between 33°S and 46°S. J. Volcanol. Geotherm. Res. 205, 114–129. https://doi.org/10.1016/j.jvolgeores.2011.03.011.

Vona, A., Romano, C., Dingwell, D.B., Giordano, D., 2011. The rheology of crystal-bearing basaltic magmas from Stromboli and Etna. Geochim. Cosmochim. Acta 75 (11), 3214–3236. https://doi.org/10.1016/j.gca.2011.03.031.

Walker, G.P.L., 1981. Characteristics of two phreatoplinian ashes, and their water-flushed origin. J. Volcanol. Geotherm. Res. 9, 395–407.

Walker, G.P.L., 1983. Ignimbrite types and ignimbrite problems. J. Volcanol. Geotherm. Res. 17, 65–88. https://doi.org/10.1016/0377-0273(83)90062-8.

White, J.D., Ross, P.S., 2011. Maar-diatreme volcanoes: a review. J. Volcanol. Geotherm. Res. 201 (1–4), 1–29. https://doi.org/10.1016/j.jvolgeores.2011.01.010.

White, J.D.L., Valentine, G.A., 2016. Magmatic versus phreatomagmatic fragmentation: absence of evidence is not evidence of absence. Geosphere 12, 1478–1488. https://doi.org/10.1130/GES01337.1.

Wilson, C.J.N., 1991. Ignimbrite morphology and the effects of erosion: a New Zealand case study. Bull. Volcanol. 53, 635–644.

Wilson, C.J.N., Walker, G.P.L., 1985. The Taupo eruption, New Zealand 1. General aspects. Philos. Trans. R. Soc. London, Ser. A 314, 199–228.

Yamamoto, T., Takada, A., Ishizuka, Y., Miyaji, N., Tajima, Y., 2005. Basaltic pyroclastic flows of Fuji volcano, Japan: characteristics of the deposits and their origin. Bull. Volcanol. 67, 622–633. https://doi.org/10.1007/s00445-004-0398-y.

Zimanowski, B., Büttner, R., Dellino, P., White, J.D.L., Wohletz, K.H., 2015. Magma-water interaction and phreatomagmatic fragmentation. Encyclopedia of Volcanoes, 2nd ed., pp. 473–484.